# Hybrid Biological-Solid-State Systems: Powering an Integrated Circuit from ATP

**Jared Marc Roseman**

Submitted in partial fulfillment of the

requirements for the degree

of Doctor of Philosophy

in the Graduate School of Arts and Sciences

**COLUMBIA UNIVERSITY**

2016

# Abstract

# Hybrid Biological-Solid-State Systems: Powering an Integrated Circuit from ATP

**Jared Marc Roseman**

This thesis presents a novel hybrid biological solid-state system which makes use of biological components in an *in-vitro* environment to produce functionality incapable by CMOS circuits alone. A "biocell" comprised of lipids and ion pumps is mated to a CMOS IC in a compact configuration and the IC is powered solely from adenosine triphosphate (ATP), often referred to as the 'life energy currency.' The biocell is a fuel cell that produces a membrane potential in the presence of ATP which is used by the IC as an electrical power supply. The design represents the first of a new class of devices combining both biological and solid-state components, which exploit the unique properties of transmembrane proteins in engineered solid-state systems. This work also suggests that the richness of function of biological ion channels and pumps, functionality that is impossible to achieve in CMOS alone, may be exploited in systems that combine engineered transmembrane proteins as biological components integrated with solid-state devices.

# Contents

# List of Figures

# List of Tables

# Acknowledgments

Many people have made this work possible. First, I would like to thank my advisor, Ken Shepard. I had originally planned to continue down the path of an integrated circuit designer during my Ph. D., however, Ken attracted me to his group after a discussion about his recent successes in bringing together biological systems with CMOS ICs. I have benefited immensely from Ken's creativity and tremendous intuition and for this I am truly thankful.

Many of the students in Ken's group come from pure circuits background we rely on each other and the post-docs to help us venture into the world of biology. I feel blessed to have had the opportunity to work with Siddharth Ramakrishnan who is not only a brilliant scientist and artist, but also a beautiful human being. Sidd's impact on my professional and personal life will be with me always. I have also benefited greatly from discussions and assistance of all of the member of the Shepard group, in particular, Matt Johnston, Jacob Rosenstein, Eyal Aklimi, Ryan Field, Sebastian Sorgenfrei, Cory Dean and Steven Warren and I would like to thank all of your for your help, support and friendship.

I am also forever thankful to my mother, for always encouraging and supporting me. I also thank my entire family, especially Aunt Linda and Uncle Neal, and Auntie Betty and Uncle Bernie and all of my cousins.

It is impossible to complete a Ph. D. without a social outlet. To my long time friend Flip Ruben, thank you for always being there for me and keeping me grounded.

I would also like to thank Chris Landry. I don't think I would have survived without all of our late night gchats. Thank you to all of the deg's; I will never forget all of our time at Am Cafe. And thank you to DDp1 for all of the fun times.

# Chapter 1

# Introduction

Nature has long been regarded as the finest of engineers. With billions of years of experience, we find uniquely creative and efficiently designed systems all around us. Of these, biological systems rank among the highest. Evolution of living systems has given rise to complex systems in nature, capable of harvesting energy from the environment, self-repair and regeneration, and an ability to sense the environment (e.g. presence of molecules [1], temperature [2], pH [3], voltage [4] and mechanical forces [5]). On a much shorter time scale, man-made silicon integrated circuits (ICs) based on complementary metal-oxide-semiconductor (CMOS) technology, have also undergone a tremendous evolution over the last 50 years. CMOS ICs form the basis for complex electronic systems with more than 10 billion transistors in a single chip. Composed of dielectrics, semiconductors, and metals, these systems are used extensively for communication and computation applications and represent the most complex engineered systems ever created. Despite this success, transformative developments and relevance of CMOS semiconductor technology will depend on new applications and new materials that reach beyond traditional communications and computation applications and beyond solid-state materials.

Solid-state devices use electrons to store and transport charge. Charge is stored

across dielectric membranes and is transported through metals. Semiconductors function as switches in the form of transistors and are turned on and off (gated) by voltage (or charge). Living systems also offer electronic devices in the form of lipid bilayer membranes, which act as capacitors, storing charge as ionic gradients across these membranes. Proteins that permeate these membranes (transmembrane proteins) act as switches (analogous to electronic transistors) and control ion transport across the membrane.

Owing to the similarities between these system and a desire to bring the functionality of each system to the other, electrical engineers and biologists often look to each other for inspiration. When electrical engineers look at biological systems, "biomimetics," a field in microelectronics that has long aspired to mimic biological systems with solid-state devices, is usually the result. One prominent example is neuromorphic computing, which attempts to imitate neural circuits in lieu of traditional Von Neumann computers [6, 7]. However, despite 40 years of efforts, including the Fifth Generation computing project in Japan in the 1980s, results have been modest at best because of fundamental differences that arise when systems are translated from "biochemical technologies" to solid-state ones. We do not "make airplanes that flap their wings" is a common metaphor for the challenges faced by biomimetic efforts.

When biologists look to electrical engineers, in particular, integrated circuit designers, they see the capability to design complex systems with tens of billions of engineered components through the almost flawless use of abstraction to manage complexity. The burgeoning field of synthetic biology seeks to build multi-component systems with functions beyond those found in nature through a combination of rational design and directed evolution [8, 9]. Synthetic biologists, who hope to create new living systems not created by evolution and who often model these systems with circuit abstractions [10], turn to abstractions used in modeling electronics in the form

of BioBricks [11] in which "data sheets" are created for biological components that can be interconnected like IP blocks on a SoC. The results are living systems, which require the functioning of many components for viability. The challenge in creating these systems is that the scientific knowledge of the biological system is incomplete, and the complexity of biological systems generally thwarts such simple efforts at abstractions and this electronics-driven approach has seen only limited utility.

The limited success of both synthetic biology and biomimetics suggests that despite their similarities, there exist fundamental differences electronic systems and biological systems. Ion channels use ions in an aqueous solution as the charge carriers while solid-state transistors use electrons (or holes) in a solid-state crystal. The electrophoretic mobility of aqueous ions (e.g. at room temperature potassium ions have $\mu_{K^+} \approx 7 \times 10^{-4}\ cm^2V^{-1}s^{-1}$ can be orders of magnitude slower than the mobility of electrons in solid-state materials $\mu_{e^-} \approx 1400\ cm^2V^{-1}s^{-1}$ .

As a result, electronic systems can switch electrons at speeds more than eight orders of magnitude faster than can be achieved with ion channels in living systems. Electronic devices can deliver switching performance well into the 100s of GHz, while ion channels are relegated to kHz switching dynamics. In terms of the mechanisms, solid-state transistors switch by raising and lowering an electrostatic barrier, blocking parts of a thermal distribution of electrons, resulting in a subthreshold slope for the resulting switch of no better than 60 mV/decade, a fundamental property of MOS transistors. The subthreshold slope indicates that a 60 mV change in the electrostatic barrier (though the action of the gate) results in an order of magnitude change in the current.

Ion channels instead switch by a mechanical conformation in the channel protein, which blocks the flow of ions. Switching is no longer governed by the subthreshold slope of MOS transistors and voltage-gated sodium ion-channels, for example, can

switch with subthreshold slopes of better than 5 mV/decade [12]. A typical membrane voltage of -70 mV, found in neurons, can cause a conductance change of greater than 14 orders of magnitude while only causing a conductance change in MOS transistors of just over one order of magnitude. Owing to the subthreshold slope, CMOS circuits generally require a minimum voltage of two to three times higher than typical membrane voltages or 150-200 mV.

Fundamental differences in component technologies, such as those described, are at the heart of the difficulties associated with both biomimetics and synthetic biology. That is, the functionality of each system is ill-tuned to the component technologies of the other. Solid-state circuits have evolved over the last fifty years to produce remarkably high gains and impressive signal-to-noise performance far exceeding those of analogous biological systems. However, functionality like the senses of taste and smell and the exploitation of biochemical energy sources are nearly impossible tasks for solid-state circuits and yet they are accomplished elegantly and regularly by living cells millions of times per day.

In order to preserve the capabilities of each system and bring the functionality of both systems together, the research in this thesis is aimed at creating hybrid engineered integrated systems that can take full advantage of both solid-state and biological components, exploiting the unique advantages of each. The engineered interaction of the heterogeneous biological with the simple, but massively integrable and robust, solid-state enables new capabilities not possible with either material system alone.

The following thesis describes the design of a hybrid system based on this principle, which brings together individual components of biology with a man-made solid-state circuit. Lipids and proteins, ubiquitous to all living systems, form the basis of a "biocell" which is mechanically and electrically coupled to the surface of a

CMOS integrated circuit, or microchip. The biocell is a fuel cell which converts the stored chemical energy in adenosine triphosphate (ATP), often referred to as "the life energy currency" into electrical energy in sufficient quantities to provide the energy required to power up the IC.

## 1.1 Thesis outline

Chapter 2 reviews the background necessary to work with and design an *in-vitro* system composed of lipids and transmembrane proteins. A comprehensive review of electrochemical membrane potential is provided along with a derivation of the total energy of thermodynamic systems based on electrochemical membrane potentials.

Chapter 3 presents the complete design biocell. Various topologies that were explored as part of the journey to the final design are described and characterized. Data that conclusively shows that the biocell is producing electrical power is presented and analyzed.

Chapter 4 presents the design of an ultra low-power, low-voltage CMOS IC for use with the biocell. Various design strategies that were employed to design an on-chip power converter with self-startup capability from 145 mV are presented.

Chapter 5 presents the complete hybrid biological solid-state system. Also included in this chapter, is a novel circuit model for ion pumps that not only predicts the currents and voltages of the entire system, but also accurately accounts for both aspects of the elecrochemical energy released by the hydrolysis reaction of ATP.

Chapter 6 summarizes the original contributions this body of work has made to the fields of electrophysiology, ATPase modeling and demonstration of an IC powered solely from ATP.

# Chapter 2

# Background and review

## 2.1 Introduction

The need for energy is universally shared by all living organisms and advances in the study of biology have produced unquestionable proof that evolution has expertly designed capabilities to provide for this need. The ability to utilize and respond to different forms of energy including light, mechanical, chemical and electrical can be found at the cellular level of all organisms in membranes that bound cell organelles and/or plasma membranes that bound whole cells. Taking various forms, this functionality can be found in the simple prokaryotic cells such as the archaea Halobacterium salinarum that can utilize light as a primary energy source [13, 14] all the way to the most complex eukaryotes that can extract chemical energy from complex molecules [15].

## 2.2 The Energetics of Life

The energetics of living systems are based on electrochemical membrane potentials (ECMPs) that are present in cell plasma membranes, the inner membrane of mito-

chondria, the thykaloid membrane of chloroplasts and others [16]. ECMPs appear due to imbalances of charge carrying ions and small molecules across the membrane. These imbalances take two related forms: concentration gradients, which produce chemical potentials, and charge separation which produce electrical potentials. That they are related stems from the fact that either one can and typically does influence the other.

Biological membranes are made of ion impermeable lipid bilayers which provide a chemical and electrical seal between the intracellular (cytoplasmic) and extracellular fluids. Lipid bilayer membranes (BLMs) act in a manner similar to electronic capacitors storing the charge associated with ECMPs. Transmembrane proteins (most notably ion channels and pumps) which span these membranes, act in a manner similar to semiconductor transistors, controlling ion transport across the membrane.

Understanding the diverse and central role of ion-channel proteins in cellular sensing, signaling and energetics has been an important area of research for many decades, and ion channels remain a major target for drug discovery [17, 18]. By controlling ion flow, ion channels can harvest energy from and respond to the environment, including detection of small molecules [1], temperature [2], pH [3], electric fields [4], and mechanical forces [19].

## 2.3 Ion Pumps

Ion pumps are responsible for establishing and maintaining ECMPs in living systems. Ion pumps can take on different fundamental structures, however they all use some form of energy to pump ions against a concentration gradient. Some examples include redox potential-driven pumps (e.g. coupling sites in the respiratory chain), light-driven pumps (e.g. bacteriorhodopsin), or bond-energy-driven pumps (e.g. ATPases).

Ion pumps which produce a net charge change across the membrane as part of

the ion transport function are known as electrogenic. Possibly the most well known of all the ion pumps is the sodium-potassium pump, or $Na^+/K^+$-ATPase. The sodium-potassium pump, which is energized by phosphorylation resulting from the hydrolysis reaction of ATP, pumps three $Na^+$ ions from the the cell cytoplasm to the extracellular matrix (efflux) and two $K^+$ ions in the reverse direction (infux). The net change in charge across the membrane is a loss of 1 q (where q is the elementary charge) as measured intracellularly. As a counter example $Na^+/H^+$-ATPases, frequently referred to as $Na^+/H^+$-exchangers, are not electrogenic because although an ionic exchange has taken place across the membrane, there is no net change in charge across the membrane.

## 2.4 Electrophysiology and Characterization of Ion Channels and Pumps

Direct electrical characterization of transmembrane proteins including both ion channels and pumps is typically performed using patch-clamp techniques [20, 21]. By direct, I am referring only to electrical measurements and excluding inferred electrical characterization by way of fluorescence techniques (e.g. voltage sensitive dyes). A curious observation can be made concerning the difference in available electrophysiolgical experimental data between ion channels and ion pumps. That is, the former far exceeds the latter. This is particularly intriguing considering that the discovery of the sodium-potassium pump (1950s) exceedingly predates modern patchclamp techniques (developed in the late 1970s). The issue is made even more curious when the importance of the sodium-potassium pump is brought to light, as evidenced by the awarding of the Nobel Price in 1997 to its discoverer, Jens Christian Skou.

A second observation is that even amongst the published experimental data

concerning electrophysiogical characterization of the ion pumps, it is glaringly obvious that there is a clear lack of voltage data (as compared to its electrical dual of current). This issue is compounded ever further when limiting the scope to characterization of ion pumps in *in-vitro* membranes.

One possible explanation for this is the fact that ion pump currents are, in general, 1000s of times smaller that those of similarly sized ion channels [22]. For the sodium-potassium pump used in this work, the ATP turnover rate, $k_{ATP}$, is approximately 100 hydrolysis events per second. With one net charge transported across the membrane per hydrolysis event, this translates to a current of approximately 16 aA. To convert this current into a voltage of 10 mV (which is reasonable in light of the noise sources of electrophysiology experimental setups) would require a resistance of $6.25 \times 10^{14}$ $\Omega$. Even if embedded into a bilayer of infinite resistance, this current would still be undetectable due to electronic amplifier limitations such as input resistance and input bias currents. As a comparison even the best CMOS opamps designed for low current measurements have input resistances on the order $1 \times 10^{12}$ $\Omega$ and input bias currents around 1 fA (e.g. Texas Instruments LMC6041).

A seemingly obvious solution then, is to attempt to make ensemble measurements consisting of hundreds of thousands of pumps operating simultaneously by patching membranes with active pumps using large micro-pipette needles. This, however, brings about an entirely new set of challenges. Larger patches directly result in lower membrane resistances. Additionally, native ion channels which present as low-resistance leakage paths must be suppressed. This approach was used to produce I-V sweeps of $Na^+/K^+$-ATPase pump currents under varying $Na^+$ and $K^+$ concentrations in [23–25] among others. In all of these experiments, various molecules were added to the patch pipette solution to neutralize the active ion channels.

An alternative approach is to make use of *in-vitro* lipid bilayers, acting as artifi-

cial membranes, in which the lipid composition is well known and the pumps could be incorporated without associated ion channels. This platform has already been shown to produce some of the fastest low-noise single-moleule ion channel measurements as of this writing [26]. When applying this approach to ion pumps, we find that like patch-clamping, it is also riddled with problems. Two of which are the difficulty in incorporating transmembrane proteins in large enough numbers to perform meaningful measurements, and that the stability of the bilayers decreases dramatically with increasing number of embedded ATPases.

One final point regarding ion pump current and voltage characterization is that despite its treatment in hundreds of textbooks and online class notes, some of the details of ECMPs as applied to biological systems are obscured by the approximation of the Nernst potential as an independent infinite energy voltage source. An attempt to add some clarity to the issue is made in section 2.6.

## 2.5 Harnessing Naturally Occurring Membrane Potentials

Recently there have been some attempts at bringing together these two systems. In 2010, Himes, et. al. observed that "complex patterns of electrical potential differences exist across the structure of a tree" [27]. By inserting steel nails into the trunk of a Bigleaf Maple tree, they were able to access potentials on the order of 100 mV, which provided sufficient voltage and power to operate a custom integrated circuit (IC). These potentials are presumably the result of ECMPs that naturally appear across the membranes of plant cells.

Animal cells (snails) also have also been exploited to produce voltages at magnitudes exceeding 0.5 V reported by Halamkova, et. al. in 2012 [28]. In this work,

biocatalytic electrodes were implanted in a snail. They demonstrated that the snail was able to regenerate glucose that was consumed by the electrodes to produce a sustainable electrical energy source. Although no attempt was made to utilize this power source, it was characterized and noted that the "electrified" snail was able to produce sustainable power exceeded 7.5 $\mu$W at 530 mV.

A more direct approach at energy extraction from animal cells was taken by Mercier, et. al. [29], who powered up a microchip from the naturally occurring endocochlear potential of a guinea pig. At approximately 30-55 mV, extraction of 1.1 - 6.3 nW of power was demonstrated. This power was harvested and used to turn on an RF transmitter.

All three of these approaches employed living systems or whole cells as a power source. This research is focused on isolating the energetics of these systems, at the component level in an *in-vitro* environment to produce a compact hybrid system.

## 2.6 Electrochemical Membrane Potential

The importance of the electrochemical membrane potential cannot be overstated. The ECMP is at the heart of the energetics and signaling of all living organisms. The ECMP is a direct result of imbalances of charge, with the chemical potential arises from concentration gradients and the electric potential from charge separation.

For any thermodynamic system in thermal and diffusive contact, the total chemical potential $\Delta\mu$, is the sum of the internal and external chemical potentials.

$$\Delta\mu = \Delta\mu_{int} + \Delta\mu_{ext}. \tag{2.1}$$

In electrochemical systems, the electric potential, $\Delta V$, appears as part of the external chemical potential.

### 2.6.1 The Units of Chemical and Electric Potential

Significant confusion can arise in electrochemical systems due to differences in the definition of the word potential with respect to chemical and electric systems. As shown below, chemical potential is a 'true potential energy' [30] having units of Joules. This comes from the definition of chemical potential which is the partial derivative of energy of the system with respect to either a single particle or a mole of that particle. Since the particles have no units associated with them, the chemical potential and the energy both have units of Joules.

This confusion is not found in electrostatic systems because we are only concerned with particles that have charge (with a well defined unit, coulombs). From a physics perspective the electric potential is the amount of electric potential energy that a unitary point electric charge would have if located at any point of space, and is equal to the work done by an electric field in carrying a unit positive charge from infinity to that point. Like the chemical potential, an electric potential is also a true potential energy, however the intrinsic reference to charge (with units of coulombs) gives rise to a new unit of electric potential, volts, which differs from the unit of energy, Joules.

A second source of confusion stems from the fact that it is mathematically convenient to talk about the energy or potential of either system alone, despite the fact that it has no physical meaning. In most treatments, the implicit reference, or point of zero potential energy, is the point of zero energy of a free particle, which is defined as equal to the zero of the kinetic energy [30]. Owing to this, and that we are only concerned properties of membrane based systems that have physical signficance, we shall only refer to differences in chemical potential, $\Delta\mu$.

For the remainder of this section we shall consider a closed thermodynamic system in thermal equilibrium consisting of two chambers (Figure 2.1), with chamber

① having $N_1$ particles and chamber ② having $N_2$ of the same particle separated by a membrane. To keep the analysis simple, the volumes, $v$ of the chambers are equal. The concentration of particles in chamber ⓘ, $C_i$, is given by $N_i/v$. In this example we use a planar membrane to separate the two compartments for clarity, however the analysis applies equally well to a spherical membrane in which one compartment exists inside the other. A gated opening in the membrane allows the exchange of particles between the system (diffusive contact).

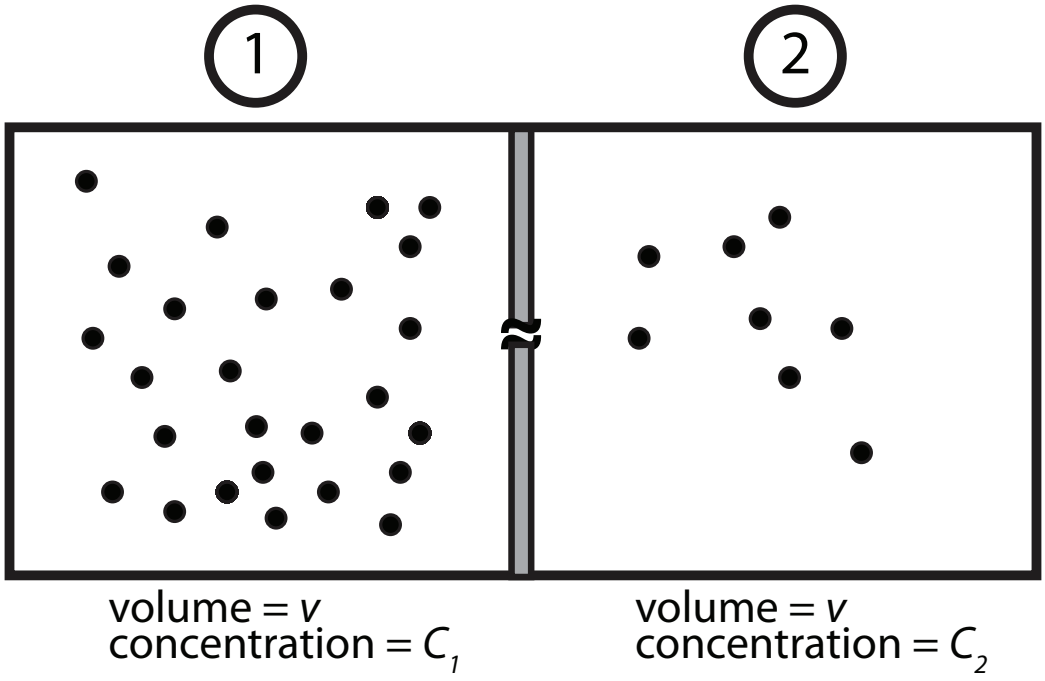


Figure 2.1: Illustration of chemical concentration gradient.

### 2.6.2 Internal Chemical Potential

The total free energy of the system in 2.1, $U$, is generally taken to be the Helmholtz free energy, however it can take on other forms by disallowing various types of work that can be performed by the system. If we disallow mechanical work, $\Delta U$ becomes $\Delta G$, the Gibbs free energy and $\Delta G$ is the total energy of the system. The total

chemical potential, $\Delta\mu$ is defined as

$$\Delta\mu = \frac{\partial \Delta G}{\partial N} = k_B T \ln\left(\frac{C_1}{C_2}\right) \tag{2.2}$$

where $k_B$ is Boltzmann's constant ($k_B = R/N_A$, where R is the ideal gas constant, $N_A$ is Avagadro's number), and T is the temperature in Kelvin. The derivation of the right hand side of eqn. 2.2 is a complicated function of the partition functions of the system and quantum concentration and is omitted for brevity, but can be found in any statistical mechanics textbook.

Since we are concerned with biological membranes in which the chambers are filled with aqueous salt solutions, we can restrict that the particles in question are charged ions, see Figure 2.2, which contains NaCl in different concentration in ① and ②. For species $i$, either $Na^+$ or $Cl^-$, the definition of equation 2.2 still applies, and we can identify the chemical potential for each species $i$ individually.

$$\Delta\mu_{int,i} = k_B T \ln\left(\frac{C_{i,1}}{C_{i,2}}\right) \tag{2.3}$$

The total internal chemical potential $\Delta\mu_{int,total}$ is the sum of the internal chemical potential of both species

$$\Delta\mu_{int,total} = \sum_i \Delta\mu_{int,i}. \tag{2.4}$$

### 2.6.3 Electric Potential

The electric potential, $\Delta V$ also comes about due to the presence of charged ions, however it is differs from $\Delta\mu_{int}$ in that it is a result of the separation of opposite polarity charges which produces an electric field, $E$.

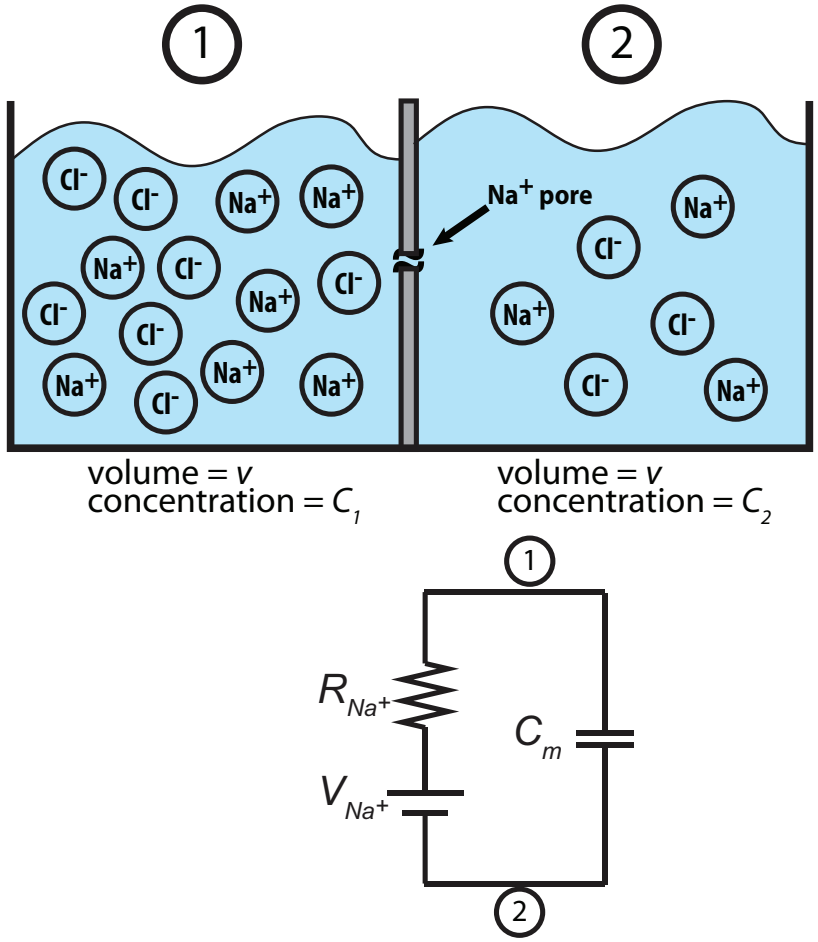


Figure 2.2: (a) Illustration of NaCl concentration gradient. (b) Electrical circuit model after $Na^+$ circuit has found thermodynamic equilibrium.

Note: The electric potential is defined as the amount of electric potential energy that a unitary point electric charge would have if located at any point in space, and is equal to the work done by $E$ in carrying a unit positive charge from infinity to that point. Thus, it is analogous to the chemical potential in that it can be defined without reference, and like chemical potential this definition has no physical significance. Therefore we are only concerned with the potential difference, $\Delta V$ of the system.

If in the system of Figure 2.2, the pore is closed and the chambers are filled with NaCl at concentrations $C_1$ and $C_2$, the system is electrically neutral and there is no electric potential, even though there is a non-zero $\Delta\mu_{int}$ as a result of the concentration gradients of $Na^+$ and $K^+$. By opening the ion-selective $Na^+$-pore (which allows only sodium ions to pass and puts the chambers into diffusive contact), we can establish the conditions under which the chemical potential gives rise to an electrical potential.

When the pore is opened, sodium ions begin to diffuse from chamber $C_1$, to chamber $C_2$. This diffusive flow of ions down their chemical concentration gradient produces an electrical current owing to the fact that each $Na^+$ ion carries with it a charge of 1 q. The diffusion of ions (electric current) is proportional to the size of the pore. If we define the pore to be a hollow cylinder, the flow of ions is proportional to $A/d$, where $A$ is the surface area of the opening and $d$ is the thickness, as derived from Fick's law. Since the membrane is only permeable to $Na^+$ ions, $Cl^-$ ions are left behind. The separation of opposite polarity charged ions gives rise to an electric field. We can calculate the electric potential associated with this field, by reasonably

assuming that the membrane is sufficiently uniform and can be modeled as a simple two-plate capacitor, with capacitance $C_m$ given by

$$C_m = \epsilon_r \epsilon_0 \frac{A}{d} \tag{2.5}$$

where $\epsilon_r$ is the relative static permittivity, $\epsilon_0$ is the dielectric constant, $A_m$ is the total surface area of the membrane and $d$ is the thickness of the membrane. The voltage $V$ across the membrane is then given by $V = Q/C$ where $Q$ is the total charge in coulombs ($+Q$ on one side and $-Q$ on the other). As sodium ions continue to diffuse across the membrane, the membrane capacitance charges up and a voltage develops across the membrane. The voltage continues to grow, however this process does not continue indefinitely. The voltage across the membrane, with chamber ② positive, induces a flow of sodium ions back across the membrane. This flow is also an electric current as each $Na^+$ ion carries electric charge with it. When the diffusive current is equal and opposite to the current induces by the developing electric field, the membrane voltage stabilizes and the system reaches equilibrium.

This can also be seen thermodynamically where the thermodynamic equilibrium is reached when the total chemical potential is zero, or

$$\Delta\mu_{int} + \Delta\mu_{ext} = 0, \tag{2.6}$$

or when

$$\Delta\mu_{int} = -\Delta\mu_{ext}. \tag{2.7}$$

Applying (2.4) to the sodium ions in the system, we find

$$\Delta\mu_{int} = k_B T \ln\left(\frac{[Na^+]_1}{[Na^+]_2}\right) \tag{2.8}$$

Applying (2.7)

$$k_B T \ln\left(\frac{[Na^+]_1}{[Na^+]_2}\right) = -q\Delta V \tag{2.9}$$

which gives us the electric potential

$$\Delta V = \frac{k_B T}{q} \ln\left(\frac{[Na^+]_2}{[Na^+]_1}\right) \tag{2.10}$$

The $Cl^-$ ionic concentration does not appear in equation 2.10 because it there is no diffusive path between for $Cl^-$ between the chambers. The presence of negative ions is however, necessary to provide the negative charge at the membrane in chamber ①. It is worthwhile to note that the current that results from the developing electric potential is also proportional to $A/d$ which makes the equation 2.10 valid for any pore size provided the conditions of diffusion as required by Fick's law are met.

Once the Nernst potential has developed, the system is in thermodynamic equilibrium, $\Delta\mu_{int} = -\Delta\mu_{ext}$ and there is no net ionic flow between the two chambers. Nevertheless, given a non-zero $\Delta\mu_{ext}$, the system can be configured to do thermodynamic electric work.

The electric potential is typically modeled by a voltage source 2.2(b) and a series resistance $R_x$ which represents the permeability or electrical conductivity of sodium ions through the pore. The membrane capacitance $C_m$ is modeled by an electrical capacitor with capacitance as defined in 2.5 in parallel with the Thevenin "Nernst" source.

We now bring to light a critical assumption that was made in the above analysis of the electric potential.

> **Assumption 1:** The change in ionic concentration before and after the pore is opened is negligible.

This can be seen in 2.10 as only the initial concentrations of the system are considered, even though there has been a net change in the total number of ions in

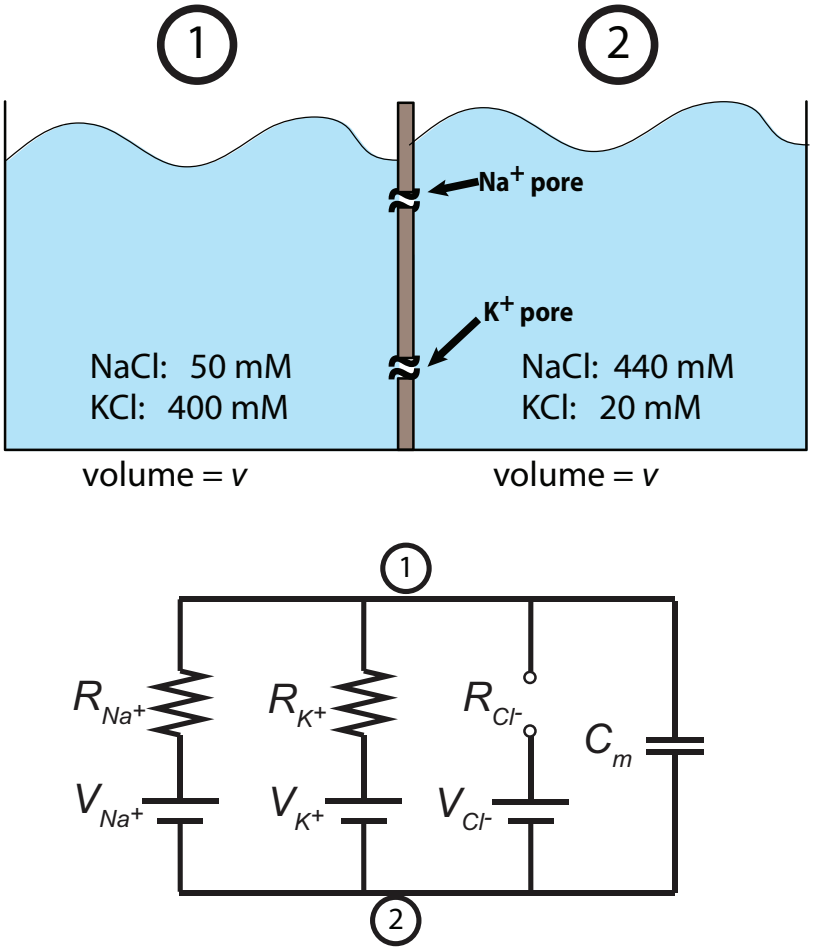


Figure 2.3: Illustration of system with two ionic species NaCl and KCl.

each chamber. The validity of this assumption can be verified via a simple numerical calculation using a typical cell volume and cell surface area. A major problem with this assumption, however, arises in systems which contain two separate ionic species in diffusive contact.

## 2.7 ECMP of Systems With Two Ionic Species

In this example, depicted in Figure 2.3, we shall use NaCl and KCl in concentrations found in a squid axon neuron shown in Table 2.1 [31].

| | ① (Intracellular) | ② (Extracellular) | $V_{Nernst}$ |
|---|---|---|---|
| $Na^+$ | 50 mM | 440 mM | -75.5 mV |
| $K^+$ | 400 mM | 20 mM | 54.8 mV |
| $Cl^-$ | 40 mM | 560 mM | -66.5 mV |

Table 2.1: Intracellular and extracellular sodium, potassium and chlorine ionic concentrations in a squid axon neuron.

The membrane is made permeable to both sodium and potassium ions with different relative permeabilities by the inclusion of ion channels of different sizes.

The Nernst potentials of both the sodium and potassium ions are modeled by Thevenin sources in parallel with each other and the membrane capacitance is modeled by capacitor $C_m$. The Nernst potentials can be calculated independently provided the concentrations are small enough to prevent electrostatic interactions as given by the debye length. The submolar concentrations of NaCl and KCl in this example are far below this critical level. The overall membrane voltage can be found by taking the superposition of each of these sources.

$$V_m = \frac{R_{Na^+}}{R_{Na^+} + (R_{K^+}||R_{Cl^-})}V_{Na^+} + \frac{R_{K^+}}{R_{K^+} + (R_{Na^+}||R_{Cl^-})}V_{K^+} + \frac{R_{Cl^-}}{R_{Cl^-} + (R_{Na^+}||R_{K^+})}V_{Cl^-} \tag{2.11}$$

Alternatively, the Goldman equation, which employs the relative permeability of each ion can be used to produce the same result.

Although the system has found a stable operating point, it is not in thermodynamic equilibrium. The composite membrane potential is different from the individual Nernst sources $V_{Na^+}$, $V_{K^+}$ and $V_{Cl^-}$, and a net current flows through each branch.

On short time scales, for typical physiological sizes and species concentrations,

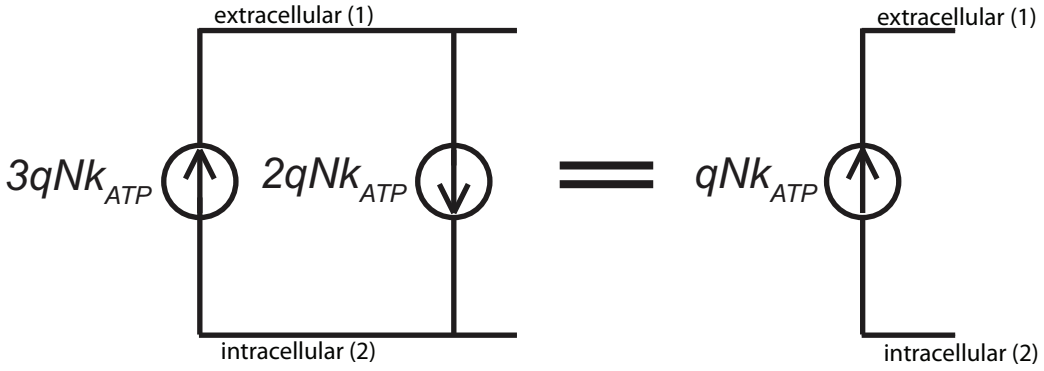


Figure 2.4: $N^+/K^+$-ATPases current sources.

we have already shown that infinite energy voltage sources based on initial species concentration are a reasonable approximation. However, in contrast to systems containing only one permeable ion which find a point of thermodynamic equilibrium, the system described here has a net current flow. Over time, the electrolyte concentration gradient will become depleted.

In the squid axon neuron that this example was based on, these concentrations are restored/maintained by $N^+/K^+$-ATPases that utilize ATP as an energy source to pump both $N^+$ and $K^+$ ions against the ECMP. Of note, is that while $N^+$ ions are pumped against both a chemical and electric potential, $K^+$ ions are pumped against a chemical potential, but fall down the electric potential.

### 2.7.1 Impact of Electrogenic Ion Pump on Electric Membrane Potential

The sodium potassium pump in our example can be modeled as two opposite facing current sources in parallel as shown in 2.4.

The sodium pump current in amperes is given by $3qNk_{ATP}$, where N is the number of active ATPases in the system and $k_{ATP}$ is the average rate of hydrolysis

of ATP in hydrolysis events per second. The potassium pump current is given by $2qNk_{ATP}$. If we concern ourselves only with the net current flow to the rest of the circuit, these can be replaced by a single current source of value $qNk_{ATP}$. As previously described the net electric current generated by the sodium-potassium pump is referred to as electrogenicity and has been characterized under various conditions [32]. By attaching the pump current source to model cell membrane is shown in Figure 2.3, we can see this source also contributes to the membrane potential given by $V_p = I_p \times R_m$, where $R_m$ is the parallel combination of all of the Thevenin resistances. Under typical physiological conditions this contribution is on the order of microvolts to single digit millivolts and is negligible compared to those of the Nernst sources.

Working in an *in-vitro* environment at the component level, we can design a membrane which contains only sodium-potassium pumps and is devoid of ion-channels. The membrane resistance $R_m$ is given only by the implicit leakage of ions through the membrane, which in our system exceeds 300 G$\Omega$. Without explicit leakage paths, the voltage produced by the pump current passing through the membrane resistance can be orders of magnitude higher than those of living cells given a sufficient number of active pumps are incorporated into the membrane. This forms the basis of the biological power source, or ATP fuel cell, that powers the IC.

# Chapter 3

# Design and Analysis of the Biocell

## 3.1 Introduction

There are many challenges associated with integrating individual biological components with solid state circuits in both the mechanical and electrical domains. For one, biological systems, and in particular living systems, tend to be soft squishy and wet. Solid-state circuits, on the other hand tend to be hard and flat and dry. Electrically, the voltages, currents and power densities of living systems and solid-state systems are dramatically disparate. This chapter is devoted to the design and analysis of the biocell, including a detailed discussion of the techniques that enabled successful integration of these two systems.

## 3.2 Designing Functional Systems with Biological Components

Working with biological components in an *in-vitro* environment presents an entirely different set of challenges than working with whole cells. Whole cells contain many subsystems to ensure continued functionality under many different environmental

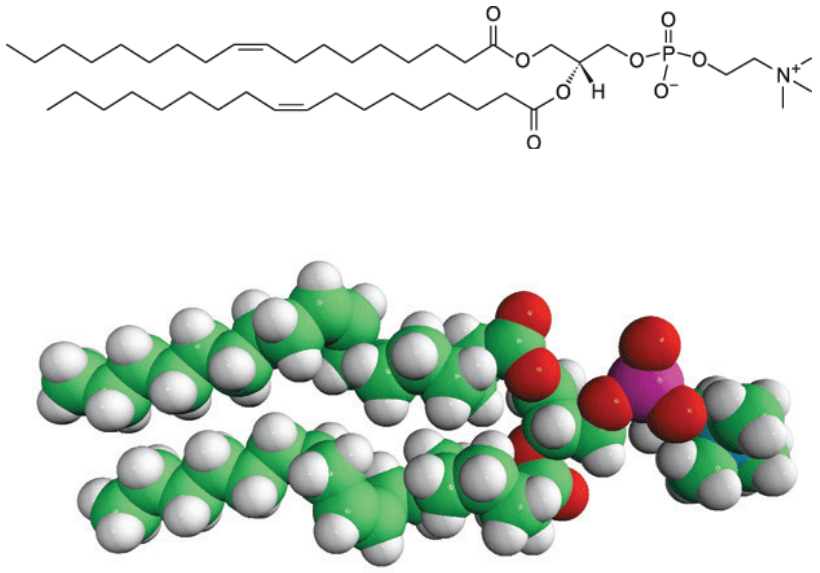

Figure 3.1: Lipid (DOPC) molecule chemical structure and illustration.

conditions. When these are fallback mechanisms are absent by design, a detailed understanding of each component, is required to produce a successful result.

## 3.3 Lipids, Micelles and Vesicles

Lipids, the main components of biological membranes, are amphiphilic molecules containing a hydrophilic (derived from the ancient greek, φίλυδρος, meaning "water loving") head, and a hydrophobic ( ὑδρόφοβος, "having a horror of water") tail [33].

In aqueous solutions, at high enough concentrations, lipids molecules form into semi-spherical geometries, either as micelles or vesicles (liposomes), by finding their lowest energy state. There is no bonding between these molecules and they are held together only by hydrophobic interactions. Hydrophobic interactions come about due to the inability of hydrocarbons to hydrogen bond with water. Both micelles and vesicles have their hydrophobic tails "protected" from solution, however they differ in that vesicles are formed from bilayers which enable solution to be present

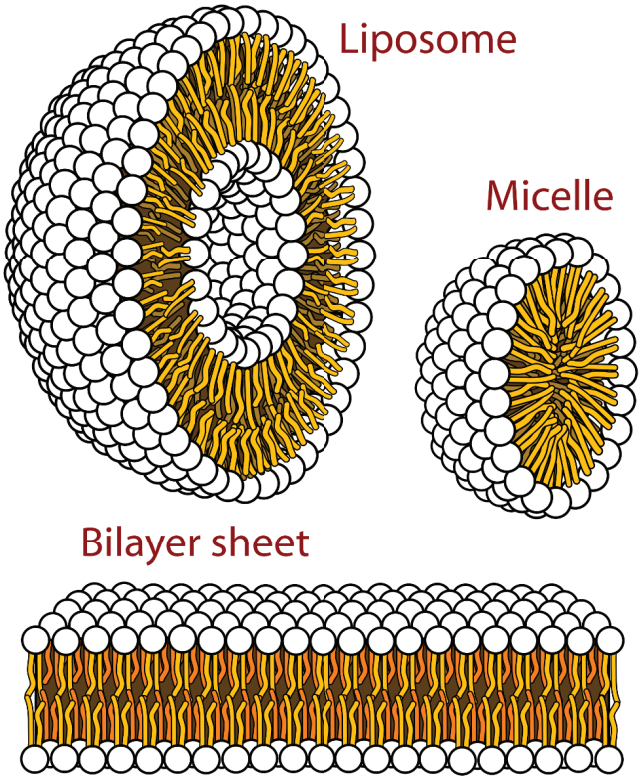


Figure 3.2: Lipid Micelle, vesicle (liposome) and bilayer illustration [35].

inside the sphere. The size and shape of both micelles and vesicles are a function of the molecular geometry of the lipids and solution conditions such as, temperature, pH, and ionic strength [34]. In eukaryotic cells, bilayer lipid membranes form the boundaries of intracellular organelles and the cell boundary, or plasma membrane.

The tightly packed lipids make bilayers highly impermeable to ions with specific resistivity on the order of $10^7 \Omega/\text{cm}^2$ [36]. Given the right environment, it is possible to unfold these bilayers into planar structures, typically referred to as black lipid membranes (BLMs). The "black" in BLM arises from the fact that since membranes are on the order of only a few nanometers, in planar configurations light that reflects back through the membrane experiences total destructive interference and

the membranes look black under a typical light microscope. Over time the acronym BLM has come to mean bilayer lipid membrane, and is used generically to refer to any lipid bilayer film.

## 3.4 Selecting a Lipid Molecule (DOPC)

Working with lipids in an in-vitro environment has been greatly simplified by the growth of commercially available purified and synthesized lipids. There are thousands of naturally occurring and artificially designed lipid molecules available for purchse. The lipid molecule employed in the final design is 1,2-dioleoyl-sn-glycero-3-phosphocholine, or DOPC for short. It is a phosphocholine lipid that has been studying at great length [37]. We now review two critical properties of lipids and why DOPC was the most attractive choice.

### Lipid/Protein Matching

Transmembrane proteins must appropriately "fold" in order to be functionally active. For this to happen, the lipid bilayer must be thick enough such that the hydrophobic domain of the protein remains "inside" the bilayer and thick enough such that the external domains of the protein actually extend past the surface of the bilayer. The hydrocarbon tail length plays a direct role in the geometry of the bilayer. Thus certain lipids and proteins are considered to be well "matched." DOPC's tail has a chain length of 18 carbons.

### Transition Temperature

One of the most important properties of a lipid bilayer is the relative mobility (fluidity) of the individual lipid molecules. Lipid bilayers typically take on two phases, a liquid phase and a gel phase and transition between the two at the transition tem-

perature. (This process is sometimes called melting and the transition temperature is referred to as the melting temperature.) The melting temperature is determined by the van der Waals forces between the tightly packed molecules in the bilayer and is primarily a function of the hydrocarbon tail length. Lipids with longer tail lengths have more surface area on which these forces can act. Working with planar bilayers below their melting temperature is not only difficult, but it is also nearly impossible to incorporate active transmembrane proteins. The transition temperature of DOPC is $-17°$C rendering it well into the liquid phase at room temperature (25°C).

| | |
|---|---|
| Molecular Formula | $C_{44}H_{84}NO_8P$ |
| Molecular Weight | 786.113 |
| Transition Temperature | $-17°$C |

Table 3.1: Summary of DOPC properties

## 3.5 Planar Lipid Bilayers

Successfully mating the biocell and solid-state circuit in a compact form requires that either the biocell take on the form factor of the chip (flat), or that the chip be made to exist in the environment native to the biology.

Lipid vesicles can be unfolded into structures known as planar bilayers, or bilayer films. The first *in-vitro* planar bilayer was demonstrated by Meuller in the 1960s [38]. Since that time the study of planar lipid bilayers has exploded due to their attractiveness as an alternative to patch-clamping for ion channel testing [39]. Currently there exist three well-established topolgies of *in-vitro* planar bilayers, each with different relative advantages [40]. These are solid supported bilayers (s-BLMs),

suspended BLMs and tethered (tBLMs).

| Attribute | Suspended | Supported | Tethered |
|---|---|---|---|
| Size | $> 10\mu$m and $< 1$ mm | No theoretical limit | No theoretical limit |
| Difficulty in preparation of substrate | Medium: requires a pore in a hydrophobic surface | Easy: clean hydrophilic surface | Difficult: Apply polymer tether (e.g. PEG, siloxane) |
| Formation of bilayer | Difficult: requires manual technique | Easy: apply vesicle solution onto surface | Depends |
| Stability of bilayer | Fragile | Very stable | Very stable |
| Incorporation of transmembrane proteins | Depends | Easy, but may be non-functional | Easy |
| Electrical contact | Easy | Very difficult | Easy |

Table 3.2: Relative comparison of attributes of *in-vitro* planar lipid bilayers

### 3.5.1 Supported Lipid Bilayers

Supported lipid bilayers are formed by allowing vesicles to sink in solution to the surface of a hydrophilic material, typically silicon dioxide. Once making contact with the surface, these vesicles undergo spontaneous fusion to form a planar bilayer [41,42].

The approach is attractive for integration with CMOS integrated circuits simply because a film of silicon dioxide can easily be grown on the surface of the chip using plasma enhanced chemical vapor deposition (PECVD). Additionally, the inte-

gration of protein is rather straightforward as the proteins can be incorporated as the vesicles are formed.

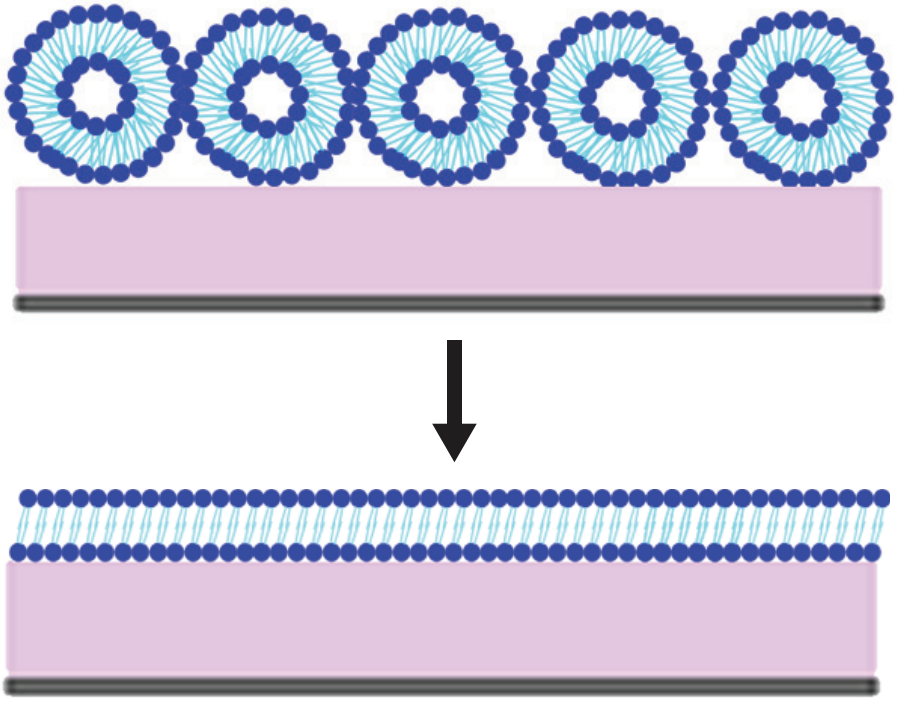

Figure 3.3: Illustration of Lipid vesicles undergoing spontaneous fusion to form a solid-supported planar bilayer.

### 3.5.2 Vesicle Formation

As previously mentioned, lipids in sufficient concentration spontaenously form into vesicles in aqueous solutions. This section reviews the details associated with cleaning and preparation of the lipids as they arrive from the manufacturer.

DOPC was purchased from Avanti Polar Lipids dissolved in chloroform (concentration 25mg/ml). Upon arrival the ampoule was cracked open and the dissolved lipids were transferred to a round bottom flask previously cleaned in “piranha” (hydrogen peroxide and sulfuric acid). The round bottom flask was placed on a Buchi

Rotavap for 5 minutes at 100 mbar. As the chloroform evaporated a thin film appeared on the bottom of the flask. The flask was then transferred to a high vacuum dessicator for two hours. The lipids were then reconstituted in various "vesicle" buffers.

### 3.5.3 Accessing the 'bottom' Side of sBLMs

In order to perform electrically characterization of sBLMs and ultimately produce electrical power, it is necessary to make electrical contact to the 'bottom' side of the bilayer. To achieve this we hypothesized that if wells of small enough diameter were etched into the silicon dioxide surface, vesicles would still spontaneously fuse into a bilayer upon reaching the surface. The following describes the prototype.

Electron beam evaporation was used to evaporate 1-$\mu$m of silver, which would eventually become the bottom electrode (electrochemistry details below). Before venting the chamber, a 50-nm film of silicon dioxide was evaporated on top of the silver. This oxide served as a passivation layer in preparation for the next step. The chip was transferred to a PECVD chamber at 300°C and 300-nm thin film of $SiO_2$ was deposited. A 300-nm layer of resist, PMMA (polymethyl methacrylate), was spun onto the chip and electron beam lithography was used to pattern wells with 200-nm diameter into the PMMA. Inductively coupled plasma was then used to transfer the resist pattern into the silicon dioxide. The resist was then stripped and the substrate was cleaned in a buffered oxide etch (20:1).

We characterized the bilayers on the substrate in two ways. First we used fluorescent tagged molecules (FITC) in a 1% concentration mixed with DOPC. This enabled us to perform FRAP (fluorescence recovery after photobleaching) experiments on bilayer. Diffusion coefficients of $3 \times 10^{-8}\,\mathrm{cm}^2/\mathrm{s}$ confirmed that a succesful bilayer formed over the wells.

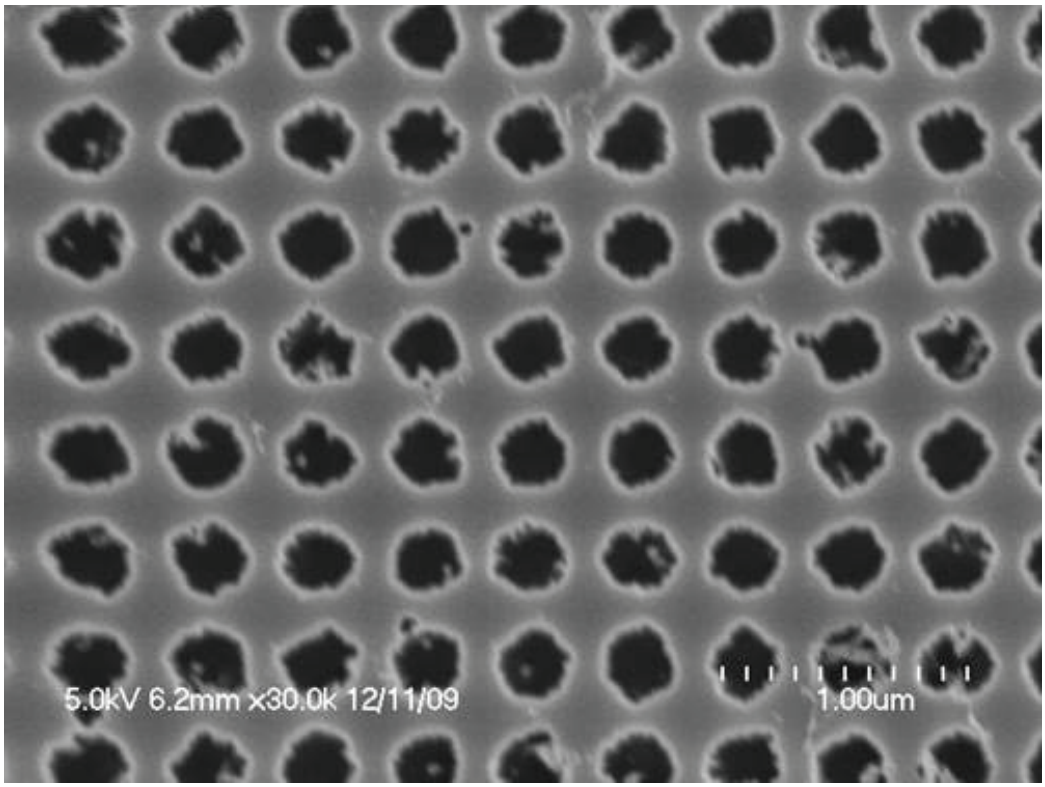


Figure 3.4: SEM micrograph of etched silicon substrate.

We were also able to confirm the presence of a lipid bilayer by measuring the DC resistance and capacitance before and after the application of lipids. DOPC is known to have a specific capacity of 0.4 $\mu$m/cm$^2$. By performing a technique known as electrochemical impedance spectroscopy, we were able to extract the resistance and capacitance of the bilayer. The capacitance was sufficiently high to prove that a bilayer was formed, however we encountered several difficulties.

First, although we were able to confirm the presence of incorporated ATPases (details described below), we were unable to detect any signal upon the addition of ATP. We presumed this to be the result of incorrect protein unfolding even over the nanowells in the substrate. A second problem was that the bilayer resistance was too low for the final application in which an electric potential of several tens of millivolts at a minimum would be necessary to power the IC. For an area of 1 mm$^2$, we were unable to improve the resistance beyond 1G$\Omega$.

There were other more practical difficulties with the patterned substrate. For one, they were incredibly difficult to fabricate. Because of the small feature size, photolithography was not an option. Electron beam write times exceeded 12 hours and this is simply not practical in a prototype environment. Furthermore, the yield was extremely low (<20%). This was due to the fact that even small defects interrupting the bilayer would present as leakage paths. Finally, we had difficulties cleaning the substrates without disturbing the metal layer below the oxide. For all these reasons, the supported bilayer approach was ultimately abandoned.

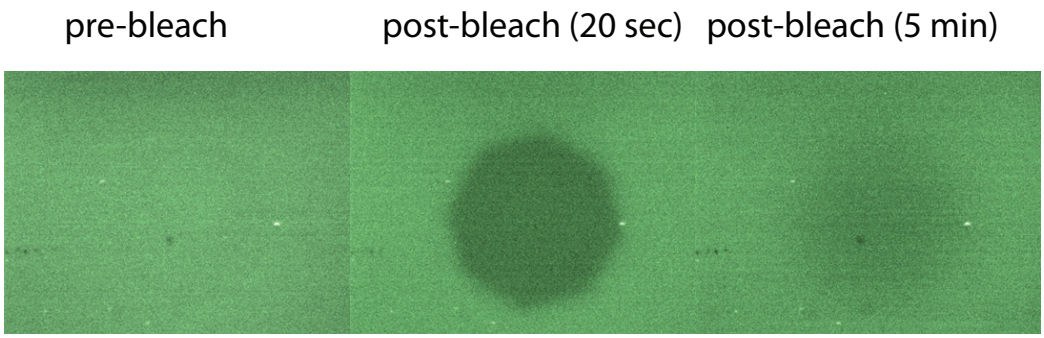


Figure 3.5: FRAP confirming bilayer on nanopatterned substrate.

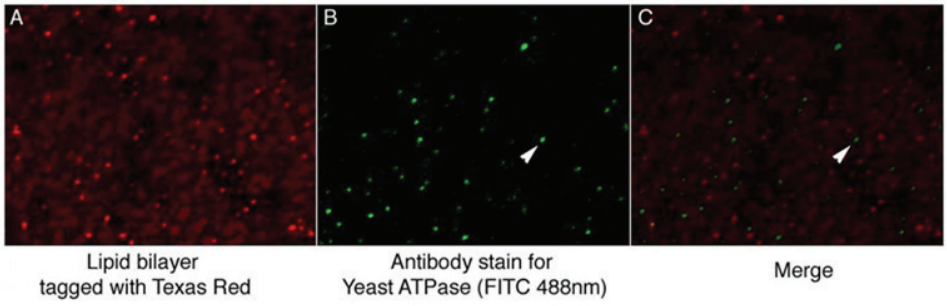


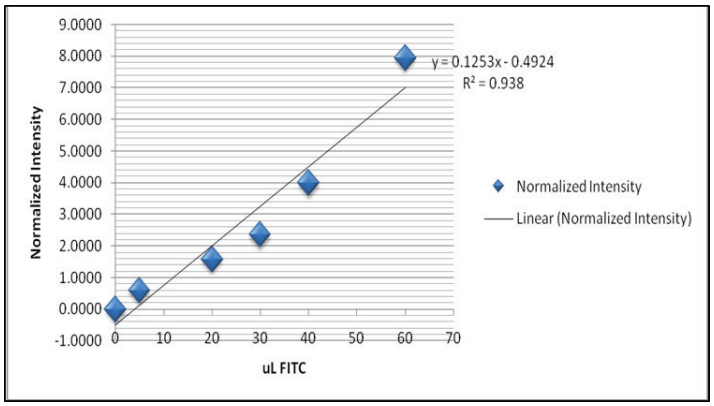


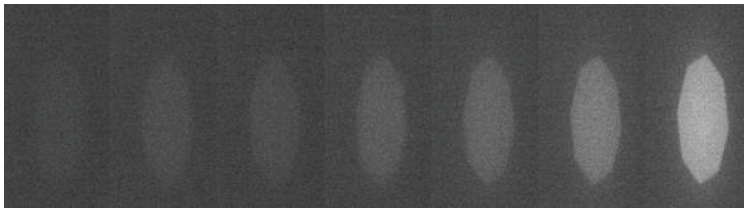

Figure 3.6: Immunohistochemistry showing ATPase incorporation in bilayer on nanopatterned substrate.

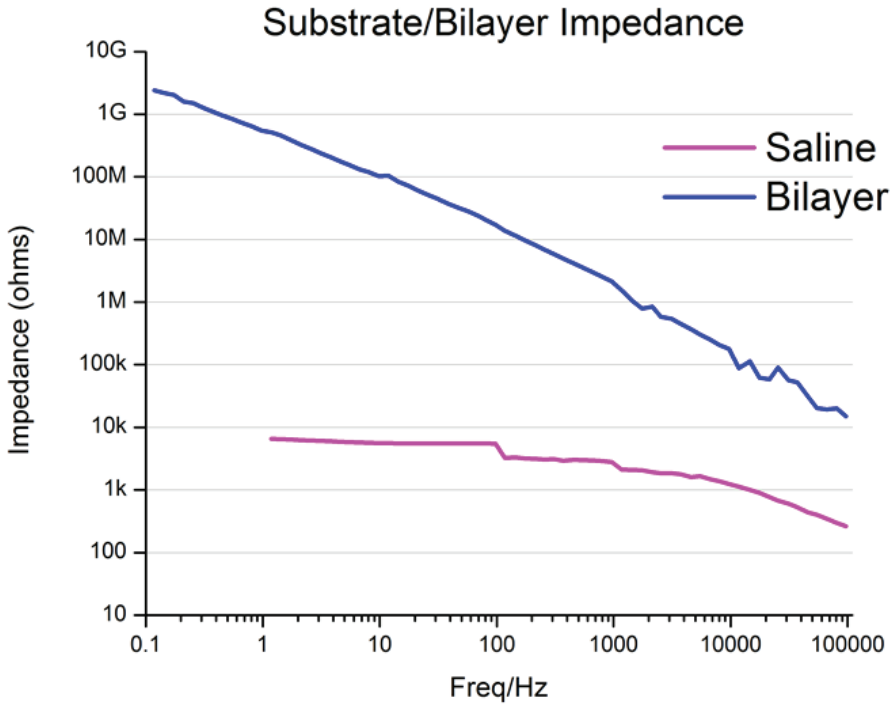


Figure 3.7: Electrochemical Impedance Spectroscopy analysis on nanopatterned substrate.

### 3.5.4 Suspended Bilayers

An entirely different architecture for planar bilayers is to suspend the bilayer across an aperture in a hydrophobic material. Suspended bilayers were actually the first successful demonstration of planar bilayers and were published by Mueller, et. al. in 1962 in their landmark publication "Reconstitution of cell membrane structure in vitro and its transformation into an excitable system" [38]. Mueller demonstrated that "by methods analogous to the formation of Hooke-Newton 'secondary black' in air soap films, a stable membrane could be formed between two compartments." Still in use today, this technique is known as 'apposition of monolayers.'

Using the same principle architecture, a second technique known as the 'painting' method can also be practiced to produce suspended bilayers. [44]. Suspended bilayers formed by the painting methods function on the principle that a 'clump' of lipids applied to a hydrophobic aperture will eventually thin away into a single bilayer. There are two main manual techniques that can be employed. The first, and aptly named technique is performed by dipping a paintbrush or a piece of teflon into lipids dissolved in an organic solvent and swiping the brush across the aperture. If the swipe was successful, a bilayer is formed over the course of a few minutes as excess lipids thin away.

The second approach is to dip a pipette tip into a solution of vesicles dissolved in an organic solvent and form an air bubble beneath the saline. The air bubble is touched to the aperture and a clump of lipids is left over the aperture. As above, over a few minutes, the excess lipids thin away and a bilayer is formed.

This technique is particularly attractive in light of the final application. The vertical suspended bilayer, can be made horizontal which can be formed on the surface of the IC. One possible way to accomplish this was presented in [45], in which planar bilayers were formed in micro-wells fabricated using the photolithographical

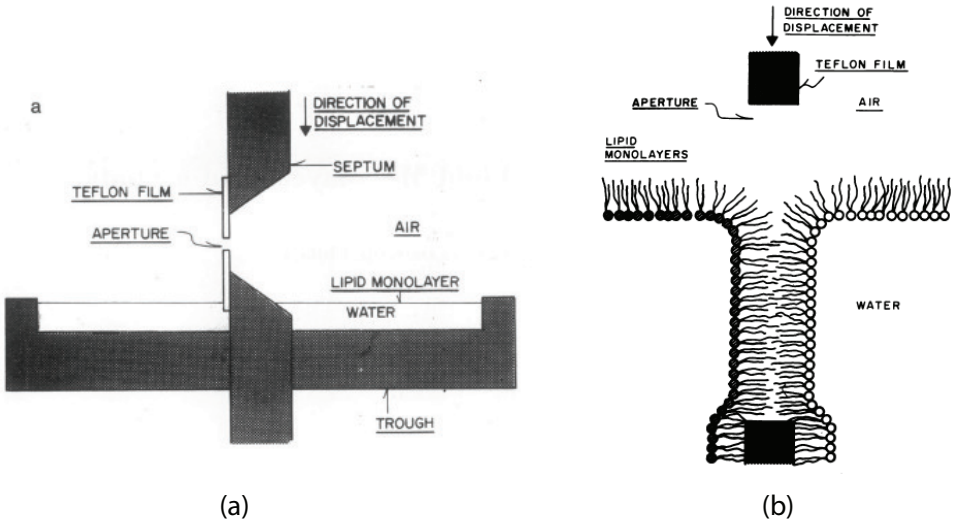


Figure 3.8: Vertical suspended bilayer architecture and formation (apposition of monolayers) originally presented by Montal and Mueller in 1972. [43]

epoxy SU-8. They showed that SU-8 was sufficiently hydrophobic that bilayers could be formed which were stable over several hours. The technology was eventually commercialized as the a product known as the Orbit-16, by the company Nanion Technologies.

We adapted the procedure to form SU-8 microwells on the surface of the IC. Electrical characterization of bilayers formed in these wells revealed that although we were able to form standard gigaohm seals, the technique could not be improved to reach hundreds of gigaohms needed to produce a voltage high enough to power the IC.

Ultimately we settled on forming horizontal bilayers in micro-machined delrin plastic in which we were able to finally able to reach a 300 GΩ target. The delrin plastic is housed in a custom teflon cell that is epoxied to the surface of the chip.

## 3.6 Sodium-Potassium Pump

The sodium-potassium pump is at the heart of the biocell design. In the presence of ATP, the electrogenic pump current in parallel with the membrane resistance creates the membrane voltage which ultimately powers the chip.

Jens Christian Skou was awarded the Nobel Prize in 1997 for his discovery of the sodium potassium pump in the 1950s. Since then, extensive characterization of the pump has revealed its role in maintaining cellular resting membrane potential as outlined in Chapter 2.

The pump operation can be broken down into six main steps in two distinct conformations (E1 and E2).

1. The pump binds 1 molecule of ATP, three $Na^+$ ions and one $Mg^{2+}$ ion from the intracellular side. (E1)

2. The molecule of ATP is hydrolyzed and the pump is phosphorylated. The magnesium ion diffusion back into the intracellular fluid. (E1)

3. The pump undergoes a conformational change from E1 to E2, opening to the extracellular side. (E1 $\rightarrow$ E2)

4. The sodium ions diffuse into the extracellular fluid and the pump binds two $K^+$ ions. (E2)

5. The pump is dephosphorylated and reverts back to the E1 conformation. (E2 $\rightarrow$ E1)

6. In this configuration, the two $K^+$ ions are released and the process begins again. (E1)

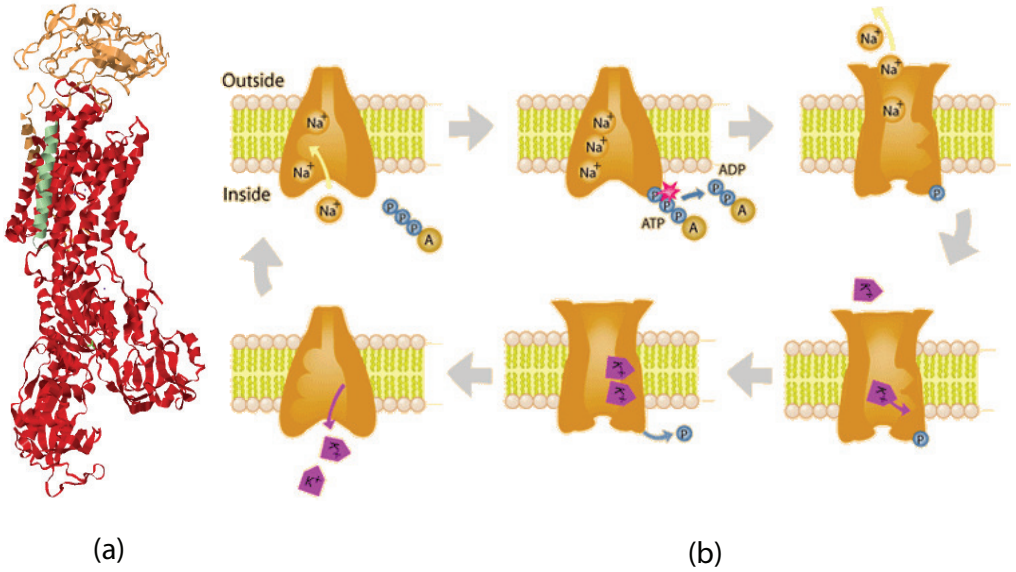


Figure 3.9: Sodium-potassium pump used in final design - ribbon illustration from protein databank. [46, 47]

## 3.7 Incorporation of the Pump Into the Bilayer

Some ion channels and pores, such as $\alpha$-hemolysin can self-assemble into the lipid bilayer simply by existing in high enough concentration in the buffer [48]. These channels are typically dissolved in an organic solvent such as ethanol and pipetted into the buffer after a stable bilayer has been formed.

Larger transmembrane proteins, like the $Na^+/K^+$-ATPase are denatured in organic solvents and an entirely different approach must be taken. A very common and well documented technique for incorporating such proteins employs vesicle fusion. The principle is that if protein-containing vesicles (preoteoliposomes) come in contact with a lipid bilayer, they will adhere to the bilayer. Divalent ions such as $Ca^{2+}$ or $Mg^{2+}$ are helpful to this end, due to the fact that the lipid heads are negatively charged. If an osmotic gradient is present between the intravesicle buffer and the experiment buffer, the vesicles will swell and burst and some of the protein will be

incorporated into the bilayer.

### 3.7.1 Formation of Proteoliposomes

Formation of proteoliposomes is an extremely challenging multistep process. Briefly, the process consists of solubilizing both the lipids and protein using an appropriate detergent. The two solutions are mixed and the detergent is extracted, leaving behind compact proteoliposomes.

The difficulty in general arises from the fact that although the general process has been shown to work, many details of the actual process at the molecular level are still unknown, for example, how the the lipids and proteins find each other during detergent extraction. Furthermore, the parameter space which includes, detergent type, lipid:detergent concentration, protein:detergent concentration, temperature, and detergent extraction method is enormous and as a result the entire process is not well characterized. Thus, for a new lipid/protein combination, a successful result could mean months, if not years, of trial and error could be required to produce a successful result.

For the purified 5'-sodium potassium adenosine triphosphatase (ATPase) from porcine cerebral cortex used in this work, the proteoliposomes are prepared prepared using a modified version of the dual-detergent protocol inspired by Alpes, et. al. in [49]. They reported that the use of dual detergents yields vesicles with higher transport activity (40-60% of original enzyme activity) than formation using either detergent alone.

#### Detailed Protocol

DOPC dissolved in chloroform (Avanti Polar Lipids) are transferred to a round-bottom flask using a glass syringe (Hamilton). Chloroform is evaporated under high

vacuum on a Buchi Rotavap for five minutes. The flask is transferred to a high-vacuum dessicator for a minimum of two hours to aid in removal of residual solvent. Vesicle buffer containing (575 mM NaCl, 5 mM HEPES pH 7.3) is added to the flask (final lipid concentration of 4mg/ml), and the flask is placed on a vortexer (2500rpm) for ten minutes. Lipid vesicles are mixed with n-Octyl-β-D-glucopyranoside (n-OG), (detergent:lipid weight ratio 3:1) and placed on a rotator for five minutes until the vesicle solution become clear. A solution of n-decyl-β-D-maltopyranoside dissolved in vesicle buffer is added to purified ATPase (detergent:protein weight ratio 3:1) and the tube is gently rotated for one minute. Purified ATPase lyophilized powder contains 90% sucrose and 0.4% EDTA. Solubilized vesicles and solubilized ATPase (lipid:protein weight ratio 5:1) are combined in 2-ml centrifuge tubes (total volume of solution 270$\mu$l) and rotated for one minute. A volume of pre-equilibrated Bio-Beads SM-2 (Bio-Rad) equal to the volume of lipid/protein mixture is added to the tubes and the tubes are placed back on the rotator. After thirty minutes the tubes are filled to the top with Bio-Beads and rotated for two hours. Proteoliposomes are removed from Bio-Beads and used immediately.

## 3.8 Silver/Silver-Chloride (Ag/AgCl) Electrodes

A pair of electrodes are necessary for accessing the membrane potential for electrical measurements and ultimately as a power source. There are several common electrode options that are typically used in electrophysiology experiments. A typical patch-clamp experiment uses a 3-electrode potentiostat configuration. A chlorinated silver wire inside the patch needle serves as the working electrode (WE) and a second silver-silver-chloride (Ag/AgCl) pellet electrode serves as the counter electrode (CE) providing a reference to the bulk solution.

The electrodes in contact with the electrolyte have a contact potential which

develops across the interface. This contact potential has a tendency to vary as the current through the electrode changes. In order to compensate for this, a third electrode, called the reference electrode (RE) is also inserted into the bulk solution. Reference electrodes also come in a variety of configurations. Two of the most common are the the Ag/AgCl reference electrode, which has a silver chloride wire in a solution of 3 M NaCl. The end of the electrode is covered with a mesh frit which allows the solution in the electrode to access the bulk solution potential, but blocks any current flow. In this configuration, although the DC potential of the bulk solution is unknown it can be well controlled experiment-to-experiment.

In our power application, the potentiostat configuration is impossible and we are left with a two electrode configuration. This presents the problem of ensuring that the contact potential between both electrodes and the electrolyte is exactly equal. In the case that they are not, the electrodes themselves can serve as an uncontrolled galvanic energy source.

The silver-chloride electrode converts ions to electrons through the following two chemical half-reactions.

$$Ag^+ + e^- \rightleftarrows Ag(s), \tag{3.1}$$

$$AgCl(s) \rightleftarrows Ag^+Cl^- \tag{3.2}$$

The overall reaction can be written:

$$AgCl(s) + e^- \rightleftarrows Ag(s) + Cl^- \tag{3.3}$$

From equation 3.3 we can see how the electrode converts ions to electrodes. At the cell anode, a chlorine ion joins with ionized silver in the bulk electrode to form AgCl. An electron carries the charge through the wire that was imparted on the electrode by the chlorine ion.

At the cell cathode, a chlorine ion leaves the silver-chloride pellet. The remaining silver ion is joined by an electron and becomes part of the bulk silver.

The low standard electrode potential $E^0$ measured against the standard hydrogen electrode (SHE), 0.23 V, makes this electrode attractive for this power transfer application. The electrode resistance in solution is at most 20 k$\Omega$ as seen in the experimental data which renders the voltage drop across this resistance negligible at the cell current levels. Finally, Ag/AgCl electrodes can easily take on different mechanical form factors, a requirement for compact integration with the CMOS IC.

### 3.8.1 Planar Ag/AgCl Electrode

Planar Ag/AgCl electrodes have been the focus of recent attention due to the advances in on chip electrochemistry [26, 50]. In [51], properties such as electrode thickness, roughness and chlorination methods were characterized under varying conditions. For current levels on the same order of those in our power transfer application, it was shown that a 500-$\mu$m silver film chlorinated chemically, using either sodium hypochlorite (household bleach) or ferric chloride, had excellent stability, varying only a few millivolts over many hours. We were able to reproduce these results, and the planar silver-chloride was evaporated onto the CMOS IC as a top layer metal to serve as the working electrode in our experiments.

## 3.9 Final Configuration of the Biocell

With each of the components established, we are now prepared to assemble a functional biocell. Figure 3.10 shows the fully hybrid biocell attached to the IC.

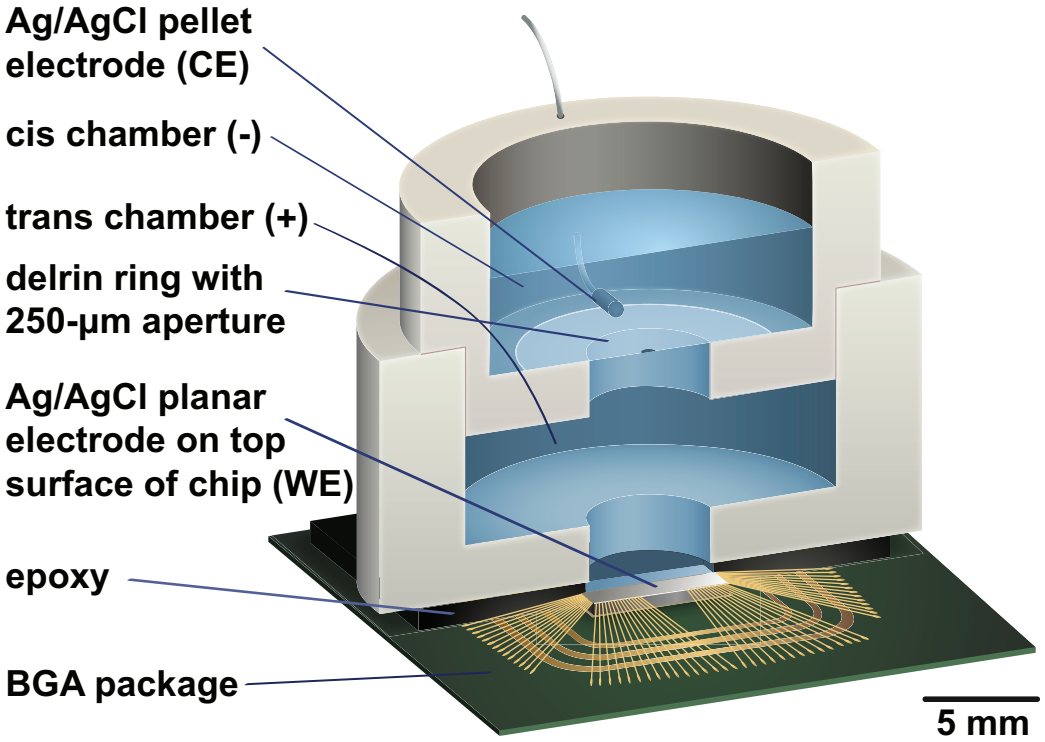


Figure 3.10: Illustration of biocell assembled to chip.

### 3.9.1 Preparation

The chip is wire bonded to a ball grid array (BGA) and donut encapsulated. The top layer of aluminum is etched away using a liquid etch and 500-nm of silver is evaporated onto the surface using electron-beam evaporation. The silver is chlorinated by the application of sodium hypochlorite for 30 minutes. The planar electrode is cleaned with 0.1% hydrochloric acid. The teflon cell is attached to the chip using a silicone epoxy (Kwik-Cast) and is allowed to set.

The lower (*trans*) chamber is filled with 1 ml experiment buffer (50mM NaCl, 10mM KCl, 3mM $MgCl_2$ and 10mM HEPES pH 7.3). A cleaned Ag/AgCl pellet electrode is inserted into the trans chamber and the electrodes are electrically shorted and equilibrate for 30 minutes. The "wire" end of the planar electrode is accessed through a pin on the BGA.

While the electrode are equilibrating, a ring made out of delrin plastic containing a 250-$\mu$m pore is attached to the upper part of the teflon chamber using a silicone epoxy. The assembly is sonicated in 40mM trisodium phosphate (TSP). After rinsing with DI water, the pore is then further cleaned by squirting 0.1% hydrochloric acid (HCl) onto both sides. This is following by a DI water rinse and then a 40mM TSP rinse. Finally the assembly is rinsed one last time under a DI water stream and dried using compressed nitrogen.

The pore is pre-treated with 1$\mu$l of DOPC lipids in n-hexane (concentration 5 mg/ml). The hexane is evaporated in a high-vacuum dessicator for ten minutes.

After the electrode have equilibrated, the upper electrode is removed and the cell is washed in DI water. The trans chamber is refilled with experiment buffer and the upper chamber with the attached pore is inserted into the lower chamber. The upper chamber is then filled with 1 ml of experiment buffer. Finally the Ag/AgCl pellet electrode is inserted into the *cis* chamber.

Using a benchtop patch-clamp amplifier, conductivity between the electrodes is verified to be $< 20k\Omega$. If this condition is not met, the cell is disassembled, and the electrode preparation procedure is repeated.

### 3.9.2 Bilayer Formation

A lipid bilayer is formed in the pore by dipping a plastic pipette tip into a solution of n-decane containing DOPC (20mg/ml), forming an air bubble by depressing the pipette plunger under the surface of the buffer in the *cis* chamber and touching the air bubble to the pore. After one minute, the bilayer capacitance is extracted by applying a voltage triangle wave and monitoring the resulting current square wave. Bilayers with capacitance less than 150 pF are reformed by touching another air bubble to the pore. The bilayer resistance is extracted by applying a series of 16 10-second

square-wave voltages from -50 mV to 100 mV in 10 mV increments while monitoring the current. The final five seconds of each step are averaged after charging-current transients have decayed away. The resistance is found by taking the inverse of the slope of a linear fit. Bilayers with resistances less than 300 GΩ are reformed. It is worth noting that if a successful bilayer cannot be formed within five tries, successive attempts are also likely to be unsuccessful, suggesting that the likelihood of formation of a high resistance stable bilayer is dependent on pore preparation (cleaning and pre-treatment).

### 3.9.3 ATPase Incorporation

Purified 5'-sodium potassium adenosine triphosphatase from porcine cerebral cortex is embedded into each bilayer by fusion of hyperosmotic proteoliposomes (2 $\mu$l, concentration 1 mg/ml) applied directly on top of the horizontal BLMs. These vesicles are formed in "intravesicle buffer" (575 mM NaCl, 5mM KCl, 10mM HEPES pH 7.3). Increased sodium ionic strength (compared to the experiment buffer) provides the necessary ionic gradient for vesicle fusion to the BLM [52].

A small amount (2$\mu$l) of very high concentration of hyperosmotic vesicles (1mg/ml) are added to the cis chamber directly on top of the horizontal bilayer. Once the bilayer inevitably breaks, it is immediately reformed with an air bubble formed using the pipette tip that was used to add the vesicles. The process continues dozens of times over three to four hours.

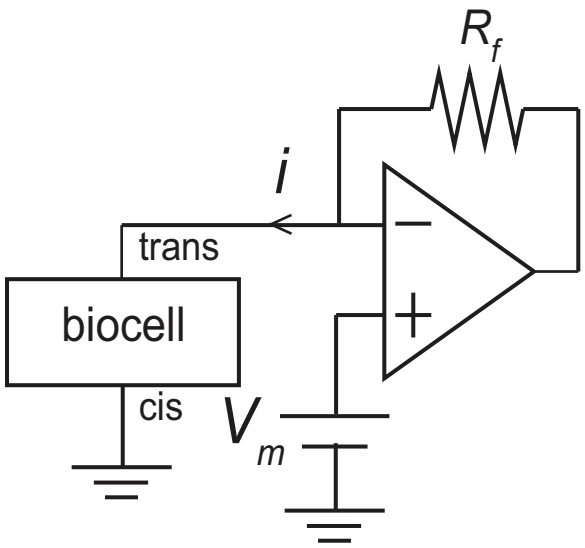


Figure 3.11: Characterization circuit schematic.

## 3.10 Experimental Results and Analysis

### 3.10.1 Measurement Setup

A HEKA EPC10 benchtop patch-clamp amplifier is used to perform the biocell characterization. The amplifier is attached in parallel to the bilayer as shown in 3.11. A second Ag/AgCl pellet electrode is used in lieu of the planar electrode on the surface of the IC.

The headstage includes 2 analog filters. The first filter is a 3-pole Bessel filter and the cutoff frequency was set to $f_c = 10$ KHz. The second filter is a 4-pole Bessel filter and the cutoff frequency was set to $f_c = 100$ Hz. The gain of the amplifier is 500 G$\Omega$.

### 3.10.2 Lipid Bilayer Characterization

#### Bilayer Capacitance and Effective Bilayer Area

The lipid bilayer is formed by dipping a plastic pipette tip into a solution of n-decane containing DOPC (20mg/ml), forming an air bubble by depressing the pipette plunger under the surface of the buffer in the cis chamber and touching the air bubble to the pore. After one minute, the bilayer capacitance is extracted by applying a voltage triangle wave and monitoring the resulting current square wave. Observing that

$$C_m = \frac{I_{C-max}}{\Delta V_m / \Delta t} \tag{3.4}$$

we can set the slope of the triangle wave to not only maximize the current output, but also prevent any additional poles from impacting the output. Figure 3.12 show the voltage stimulus (blue) and resultant bilayer current. The triangle slope is 5, and $I_{C-max}$ is 765 pA, resulting in a membrane capacitance of $C_m = 153$ pF. Using the specific capacitance of DOPC, $0.4\mu\text{F/cm}^2$ [53], and the area of $4.91 \times 10^{-4}\,\text{cm}^2$ for a circle with a diameter of 250 $\mu$m, we would expect a capacitance on the order of 250 pF. However due to excess lipids at the boundary of the pore, the effective bilayer area is only $\sim 65\%$ of the total pore area.

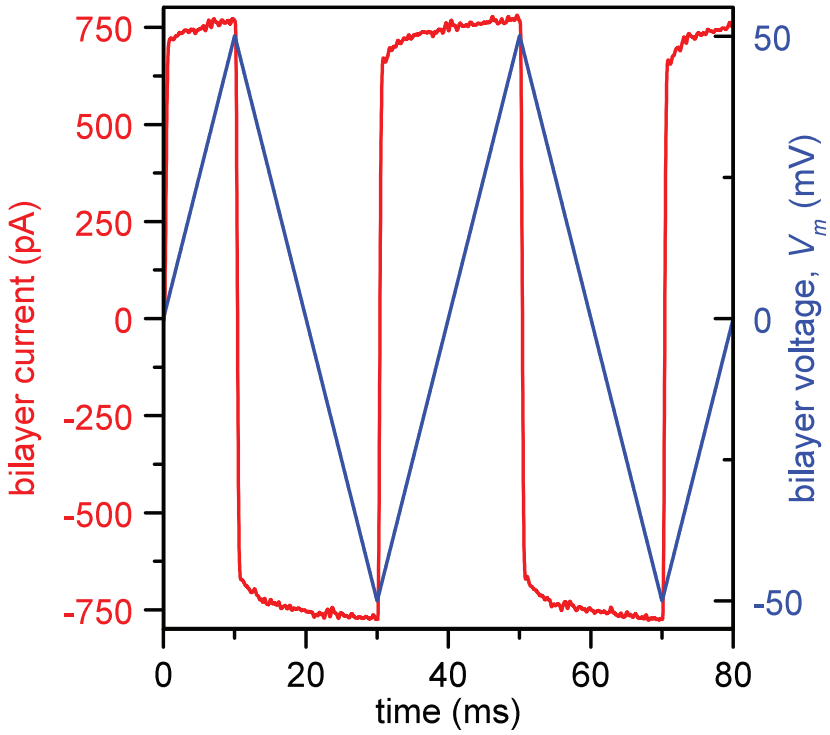


Figure 3.12: Biocell capacitance measurement.

**Bilayer Resistance**

Bilayer resistance is typically measured by applying applying a voltage step and measuring the DC current through the bilayer after the charging current has dissipated. This works well for bilayers on the order of 1-10 GΩ and an amplifier with input bias currents on the order of 100-300 fA. For bilayers exceeding 100 GΩ, an applied voltage of 100 mV results in a current of 1 pA. At these levels, the amplifier non-idealities produce errors exceeding 10%. To calibrate out these errors, a series of 16 voltage steps, from -50 mV to 100 mV (10 mV increment, 10 s in length) are applied to the bilayer. The final five seconds of each step are averaged after charging-current transients have decayed away. The resistance is determined to be the inverse of the slope of a linear fit. These measurements are shown in 3.14.

## 3.11 Post ATP Measurements

After ATPase incorporation has taken place as outlined above, and ATP is added to the biocell, final concentration 3 mM, the cell produces electrical power.

### 3.11.1 Short Circuit Current

Upon adding ATP to the biocell (*cis* chamber), final concentration 3 mM, a 1.7-pA short circuit current is observed. The current takes $\sim$ 100 seconds to stabilize. This is presumed to be related to the time it takes for the ATP to diffuse down to the bilayer. The short-circuit current is shown in 3.13(a).

### 3.11.2 Biocell Open Circuit Voltage

The open circuit voltage is shown in Figure 3.13(b). The cell was initially externally shorted and then subsequently opened at $t = 0$. The resulting voltage was measured

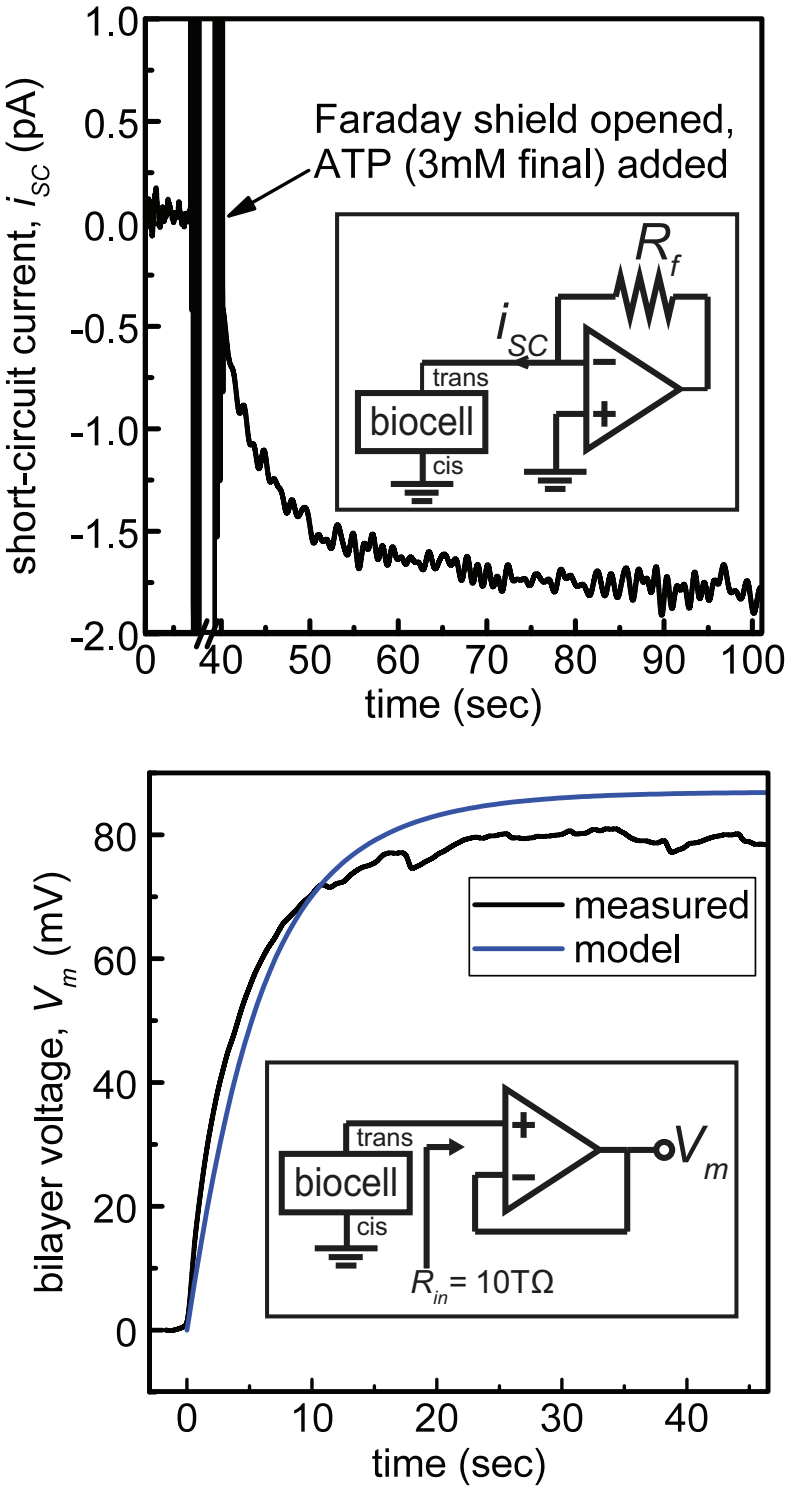


Figure 3.13: Biocell short circuit current and open circuit voltage response to 3 mM ATP to the cis chamber.

using a custom amplifier with input resistance $R_{in} = 10$ T$\Omega$. The superimposed model parameters are derived below.

### 3.11.3 I-V Characterization

Once the short circuit current has stabilized, an I-V sweep of the biocell is performed. Figure 3.14 shows the complete measured current-voltage (I-V) characteristic of a single ATPase-bearing membrane in the presence of ATP. The current due to membrane leakage through $R_m$ is subtracted in the post-ATP curve. The same voltage clamp amplifier configuration used to measure the response of 3.11 is employed here but with varying applied bias ($V_m$) across the membrane. When biased in the fourth quadrant, the biocell produces electrical power. The I-V characteristic fits a Boltzmann sigmoid curve,

$$i = i_{sc} + \frac{-i_{sc}}{1 + exp\left(\frac{V_m|_{i=i_{sc}/2} - V_m}{\alpha}\right)} \tag{3.5}$$

where $\alpha$, the Boltzmann "slope factor", is 0.02 V, consistent with sodium-potassium pump currents measured on membrane patches at similar buffer conditions [**?**, 32, 54], and $i_{sc}$ is the short-circuit current. This non-linear behavior reflects the fact that the full ATPase transport cycle (three $Na^+$ ions from cis to trans and two $K^+$ ions from trans to cis) time increases (the turn-over rate, $k_{ATP}$, decreases) as the membrane potential increases [54]; that is, the pump consumes less ATP and the current decreases with increasing membrane voltage.

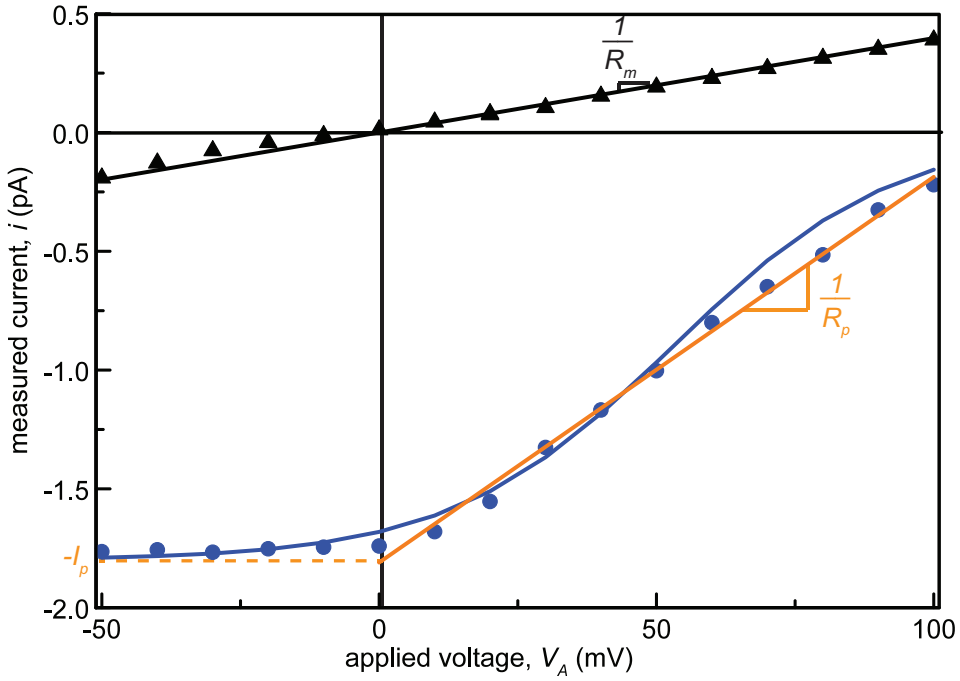


Figure 3.14: Single cell biocell characterization. (A) I-V sweeps of biocell before (▲) and after (●) addition of ATP (3mM final concentration). Voltages are stepped for this measurement. Bilayer current is the average of the last five seconds of a 10-second step (after charging currents have decayed away). Pre-ATP data linear fit (–) slope yield $R_m$ = 280GΩ. Post ATP data fit to a Boltzmann curve, slope = 0.02 V (–). Post-ATP linear fit (–) yields $I_p$ = -2.1 pA and $R_p$ = 61.6GΩ. Transimpedance amplifier gain is 500 GΩ. The headstage filter consists of a three-pole analog low-pass Bessel filter $f_c$ = 10 KHz in series with four-pole analog low-pass Bessel filter $f_c$ = 100 Hz. Data is post-processed with a low-pass digital filter with $f_c$ = 1 Hz.

## 3.12 Biocell Circuit Models

Using the Boltzmann fit for the ATPase I-V response described in section 3.11.3, we can design a non-linear circuit model for the ATPases. The clear dependence on $V_m$ indicates that a non-linear voltage-controlled-current-source can be used in place of the simple DC source of Chapter 2.

Using a polynomial fit, the first four coefficients of a polynomial expansion were used in the dependent voltage source shown in Figure 3.15(a). In the fourth quadrant, this model can be linearized (Figure 3.15(b) as a Norton equivalent circuit, consisting of a DC current source ($I_p$) in parallel with a current-limiting resistor ($R_p$), which acts to limit the current delivered to the load at increasing bias ($I_{ATPase} \sim I_p – V_m/R_p$).

Although the non-linear circuit model is numerically more accurate, the linear circuit model can be used to analyze parameters such as maximum power transfer and efficiency when using biocell as a power source. This is shown in Chapter 5 where the complete hybrid system is presented.

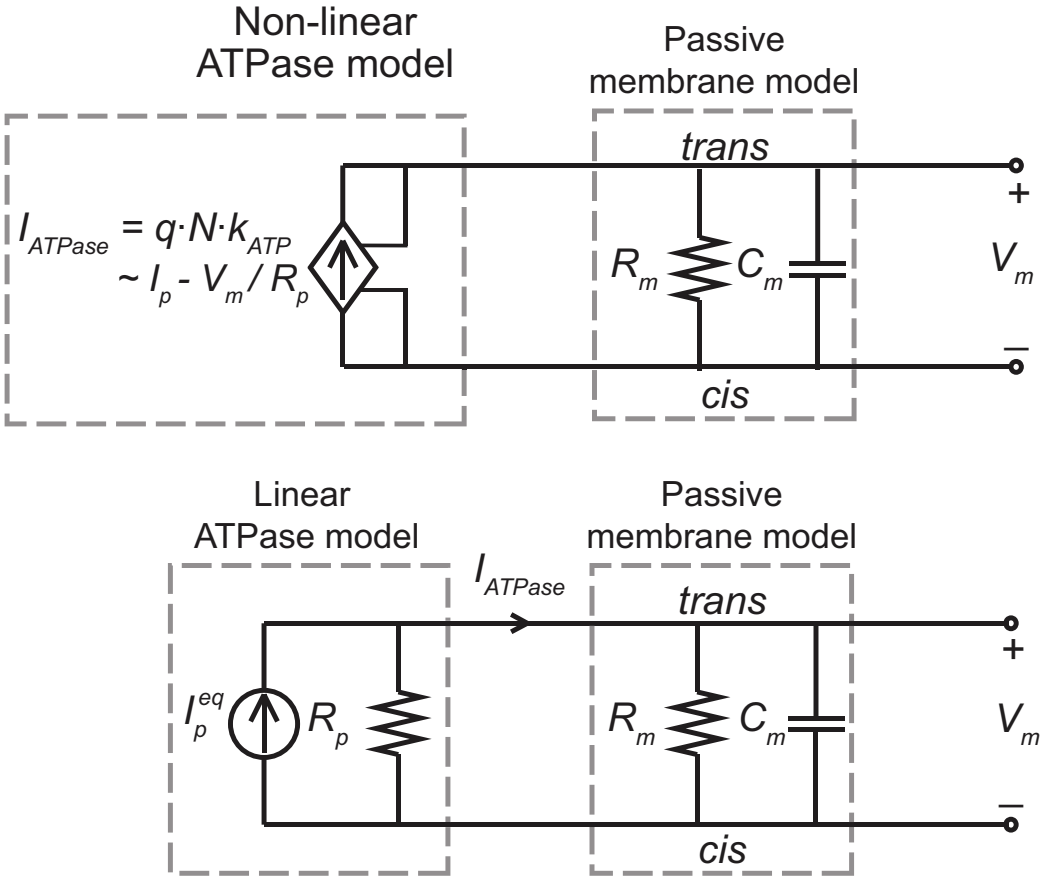


Figure 3.15: ATPase electrical circuit model based on I-V characterization data. (a) Non-linear circuit model using a dependent current source for the ATPase branch. (b)Linearized Norton equivalent circuit model.

## 3.13 Chapter Summary

This chapter described each component of the design of the biocell in detail. The final architecture was presented and an electrical circuit model was developed for the ATPase which was shown to accurately predict the open-circuit voltage response of the system.

# Chapter 4

# Design of an Ultra-low Power Ultra-low Voltage Power Converter CMOS Integrated Circuit

## 4.1 Introduction

Making efficient use of biological systems as electrical power sources brings about a very unique set of circuit design challenges. We have entered the worst paradigm for a circuit designer, which is to exist in the space where two requirements are placed on the design and these requirements are exact trade-offs with one another. Specifically, we are referring to design where the voltage and power are both extremely low by CMOS standards are fixed by the output of the biocell.

The *in-vivo* designs presented in [27] and [29], used CMOS IC loads to demonstrate that the biological power source can be used to do electrical work. Both designs used on-chip power converters to make use of the biological power source. These designs were plagued, however, by the need for an external power source to "kick-start" the on-chip power converter.

In this design, implemented in a standard 0.45-nm CMOS SOI process overcomes this problem. The power converter is capable of self-startup from 145 mV and can support sustained operation with input voltages as low as 110 mV at apower conversion efficiency exceeding 70%.

## 4.2 Typical Voltages of Biological Systems and Solid-State Systems

The electrical characteristics of biological systems and solid-state systems are mismatched in their operating voltages. The minimum operating voltage of solid-state systems is determined by the need for transistors to modulate a Maxwell-Boltzmann (MB) distribution of carriers by several orders of magnitude through the application of a potential that is several multiples of $k_BT/q$. Biological systems, while operating under the same MB statistics, have no such constraints for operating ion channels since they are controlled by mechanical (or other conformational) processes rather than through modulation of a potential barrier.

## 4.3 Design Requirements Based on the Biocell

The following design requirements have been extracted from the detailed biocell characterization in Chapter 3. These can be summarized quite easily as the output voltage of the biocell, which is $\sim$80 mV, and max power output of 148 fW.

## 4.4 Switched Capacitor Voltage Doubler

To bridge the operating voltage mismatch between the biocell and the minimum operating voltage of transistors, the primary circuit on the chip is a switched-capacitor

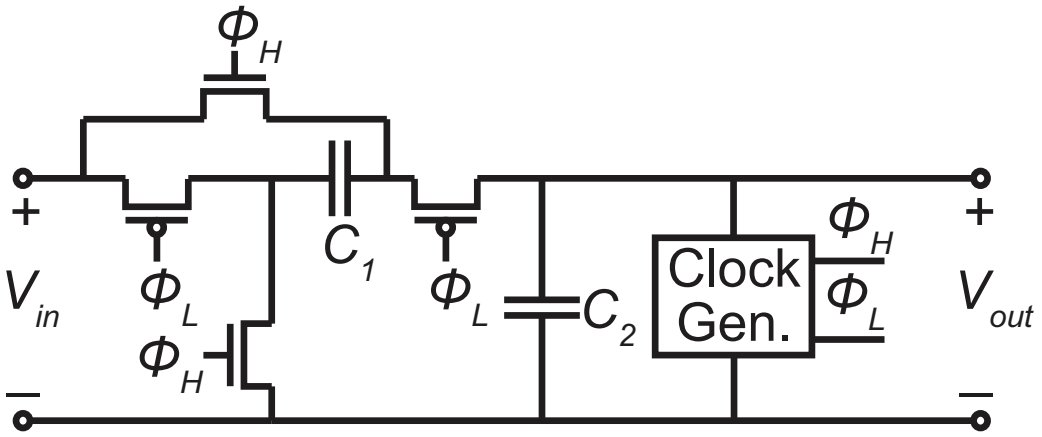


Figure 4.1: Switched-capacitor voltage doubler circuit schematic.

(SC) voltage doubler, shown in Figure 4.1. The (SC) voltage doubler at its core resembles other SC designs, however associated circuitry is necessary for self-startup and sustained operation at sub-200 mV input sources.

### 4.4.1 Converter Steady-State Operational Details

After starting up, flying capacitor, $C_1$ = 100 pF, is charged up to the input voltage when the NMOS transistors are on. When the PMOS transistors are switched on, it is stacked in series with the input and attached to output capacitor, $C_2$= 100 pF. Deep-trench (DT) capacitors, which are available in this process are employed as the flying and output capacitors $C_1$ and $C_2$ [55]. DT capacitors are used in memory design and have remarkably densities on the order of $0.2\mu\text{F/mm}^2$, which comes at the expense of high series resistance [56]. The intrinsic time constant of the 100 pF capacitors used in the design is $10\mu$s. For typical on-chip converters which can switch into the GHz regime [57], these capacitors could not be used, however, at the switching frequencies employed in the design, the impedances far below that which they begin to lose their capacitive behavior.

### 4.4.2 Clock Generator

In steady-state operation, the clocks to run the converter are generated by a trimmable five-stage ring oscillator. Transistors with nominal threshold voltages, $|V_{T,lin}|$ of 760 mV are employed. The trimming capacitors are necessary to contend with large process variability. They can also be used to select $f_{clk}$, the unloaded switching frequency of the converter. They are switched in using pass gates controlled by an external 1.5-V supply brought onto the chip specifically for this purpose. In an autonomous configuration (in which the 1.5-V supply is not available), these could be trimmed with fuses.

The core clock generator is shown in 4.2. In a typical SC converter, non-overlapping clocks are used for each of the phases [58, 59], however simulation reveals that the additional switching logic necessary to support non-overlapping clock generation ($> 20$ nW) outweighs the loss due to short circuit currents ($< 3$ nW). Alternating phases are achieved using a single-phase clock driving complementary switches.

### 4.4.3 Start-up Oscillator

The steady-state oscillator frequency is too slow to start the converter from the target $V_{in}$ of $5.5\ k_BT/\mathrm{q}$ necessitating a separate startup ring oscillator of identical architecture, formed with lower $V_T$ devices (nominal $|V_{T,lin}| = 565$ mV). The switches must be switched fast enough that any progress (increasing voltage) made during one phase is not lost to leakage during the other, and that it must be slow enough such that power dissipated in charging gate capacitance does not decrease the output voltage by any more than is gained in one cycle. Simulation predicted reliable start-up at $V_{in}$ = 125 mV considering process and random variability. Measured converters showed reliable startup at $V_{in} = 145$ mV due to the realization of slower devices than those predicted by the transistor compact models.

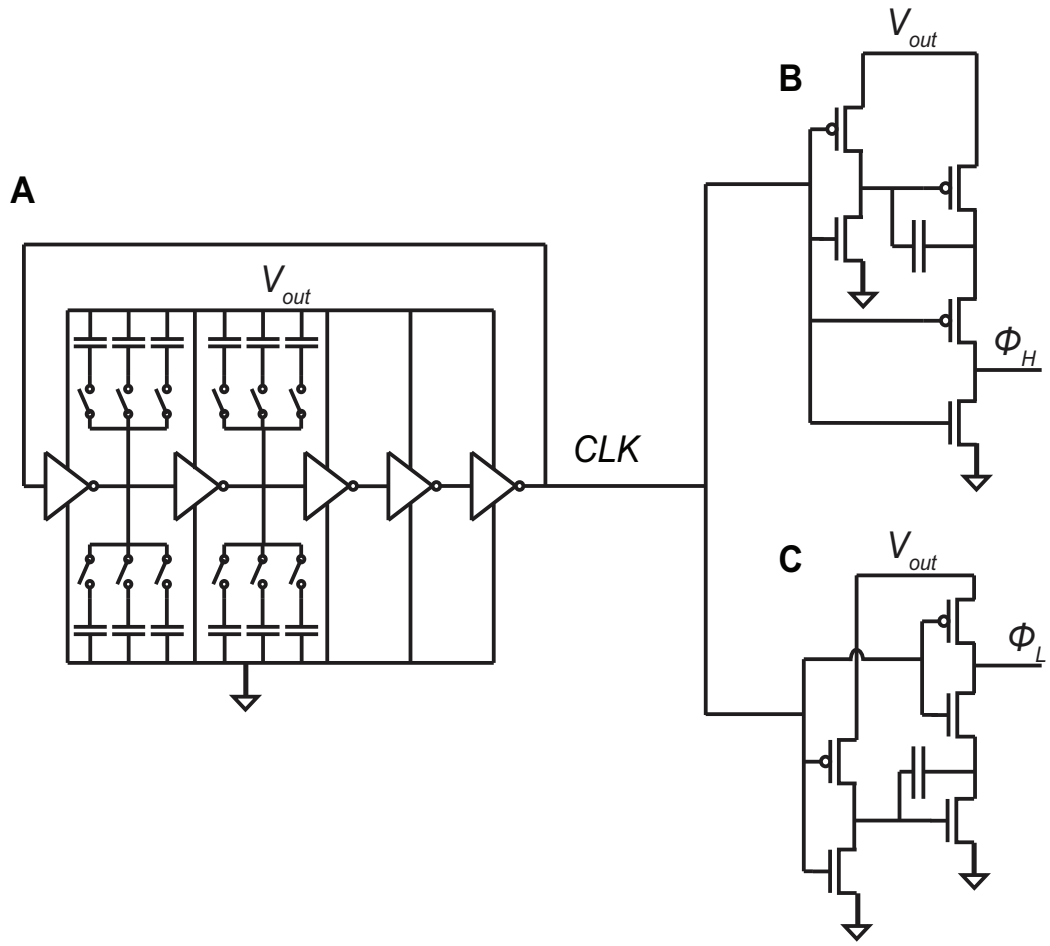


Figure 4.2: Steady-state operation clock generator circuit schematic.

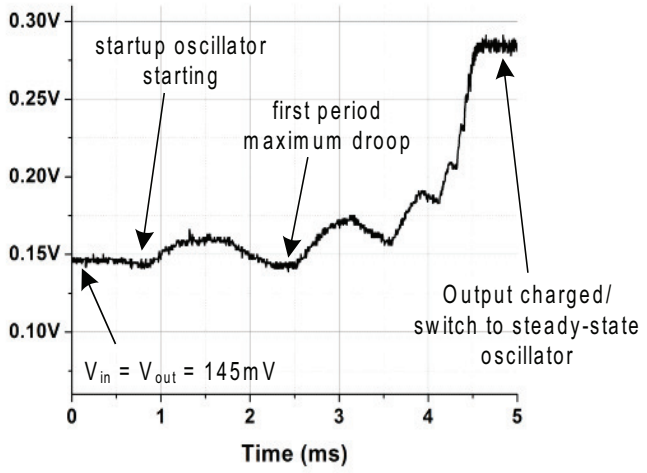


Figure 4.3: Converter startup transient.

### 4.4.4 Boosting the Gate Drive of the Core Switches

In order to increase the $I_{on}/I_{off}$ ratio of the switch transistors in the converter, the single-phase clock output of the oscillator is bootstrapped (boosted) to provide higher gate drive as shown in Figure 4.4. In steady-state (for $V_{in}$ = 150 mV), the boosted positive clock (for driving NMOS switches) of 480 mV and boosted negative clock (for driving PMOS switches) of -200 mV. Steady-state $I_{on}/I_{off}$ ratios of the devices are increased almost ten-fold from 4600 to 40,000, reducing conduction losses due to switch on-resistances. The bootstrap driver was critical in starting up the converter. At $V_{in}$ = 4.5 $k_BT/q$, the $I_{on}/I_{off}$ ratio was increased from 30 to over 1200. The bootstrap drivers were so critical that no startup frequency could be found without the use of the bootstrap circuit. An additional increase in transistor transconductance is achieved by using body-contacted devices and shorting the gate to the body in a dynamic-threshold configuration [60].

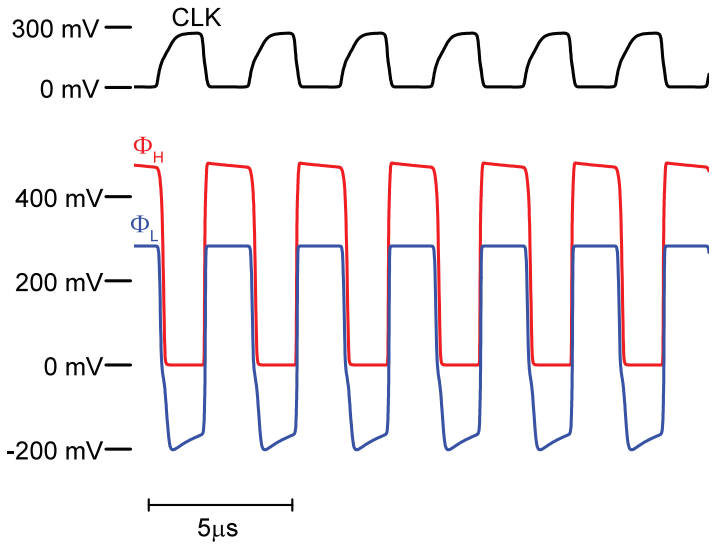


Figure 4.4: Clock bootstrap.

### 4.4.5 Output Load Regulation and Output Resistance

To maintain high efficiency at input power levels in the nanowatt regime, it was necessary to forego output load regulation. Increasing output ripple and decreasing average output voltage with increasing load is observed. The non-zero output resistance, given by $R_o \approx \frac{1}{f_{clk} C_1}$, can be minimized by increasing $f_{clk}$. The measured $R_o$ is larger than this value because the output voltage droop decreases the actual switching frequency. Maximum efficiency is achieved when the switching frequency is reduced to the maximum tolerable output ripple. The resulting efficiency as a function of output load power, $P_{load}$, is shown in Figure 4.5.

### 4.4.6 On-chip Test Circuits

The design includes 15 calibrated current sources that are used to load the converter. An reference on the board is brought onto the chip. The chip can be configured

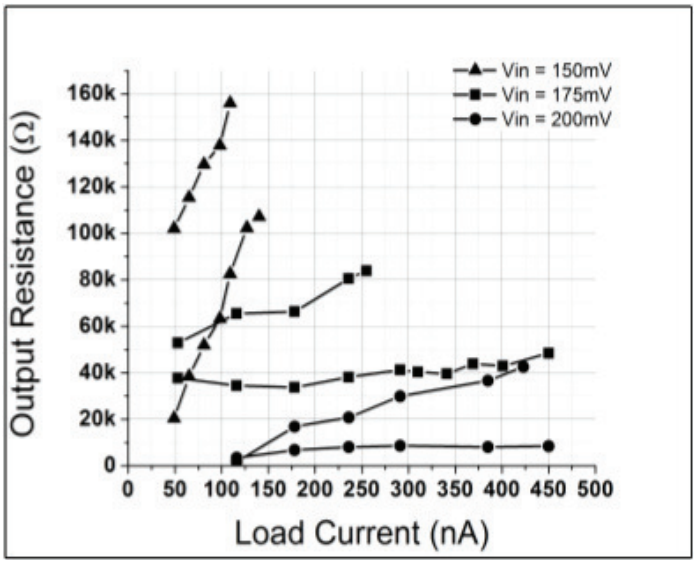


Figure 4.5: Output Resistance as a function of load current.

into calibration mode, in which the various current sources can be brought back off the chip. The sources use a standard self-biasing network topology. Due to process variation, and that the devices were operating in sub-threshold, it was necessary to calibrate the sources for converter that was tested.

### 4.4.7 Ring Oscillator Loads

The design includes four independent ring oscillators (2-11 stage and 2-31 stage) comprised of extra high threshold voltage (XVT) transistors, which can be switched in the output. The ring oscillators represent the switching action of a typical digital logic processor. The output of these four oscillators is shown in Figure 4.6.

## 4.5 Efficiency Analysis and Results

To determine the efficiency of the converter ($\eta_{converter}$), we must account for power losses in the converter that include both conduction losses ($P_{cond}$) and switching losses

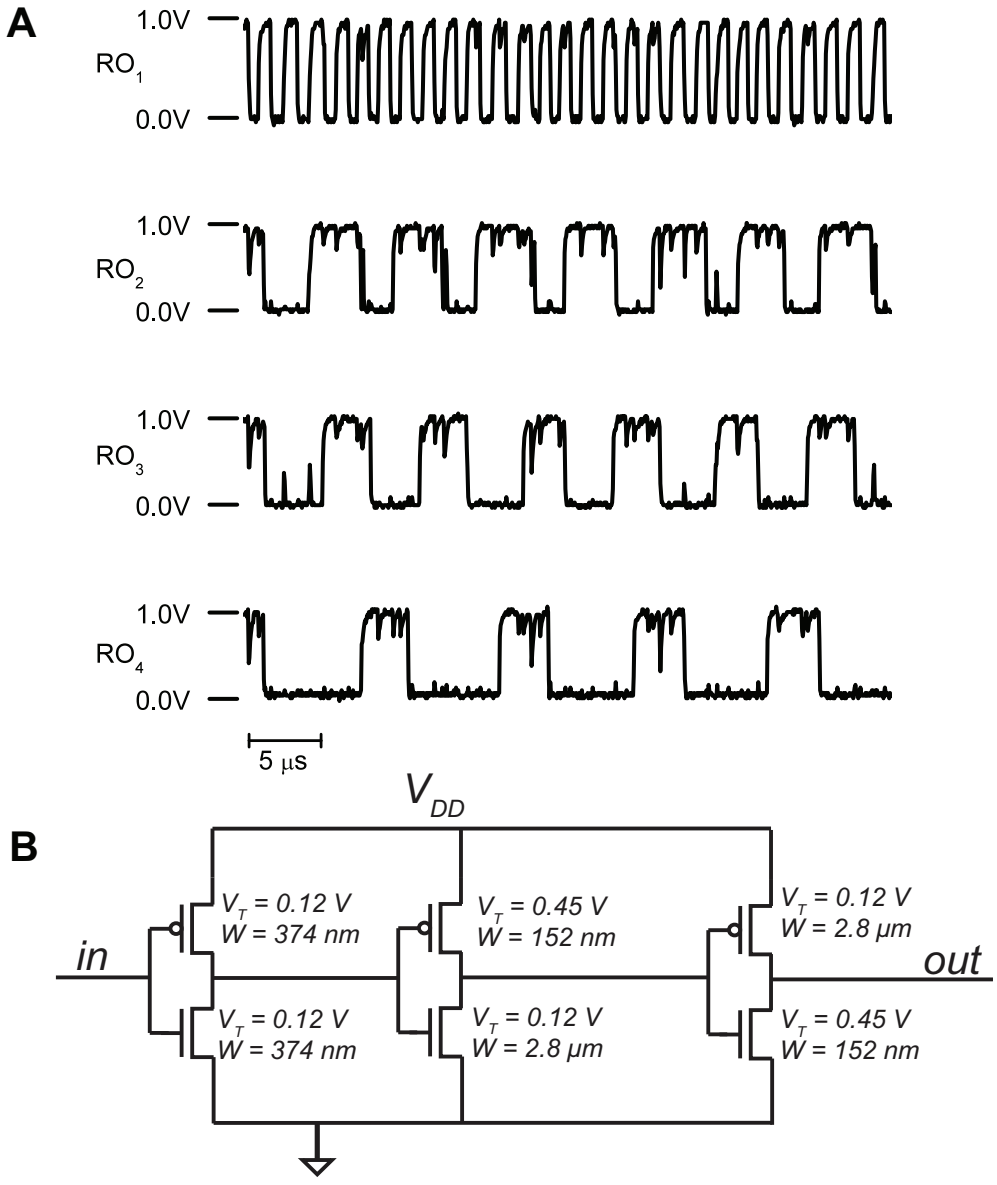


Figure 4.6: Four independent ring oscillators running off the output of the power converter.

($P_{sw}$) [59]. The losses associated with any additional control circuitry including clocks, have been lumped in with Psw, due to their strong dependence on clock frequency. Maximizing efficiency in the ultra-low power regime necessitates that the design be tuned for a specific target source $V_{in}$, in this case 150 mV (which is approximately twice the voltage of the biocell). The design performs well in a small range of inputs around the target source but efficiency quickly drops when $V_{in}$ is more than 200 mV. This limited range is due mostly to the exponential dependence of transistor currents on node voltages in the subthreshold region.

The converter efficiency under varying loads is shown in 4.7 at the average voltage input of the biocell (135 mV).

## 4.6 Chapter Summary

This chapter described the design of an ultra low-power low-voltage CMOS IC for use with biological power sources. We presented a switched-capacitor voltage converter necessary to match low voltage biological sources with the minimum operating voltage of standard CMOS transistors.

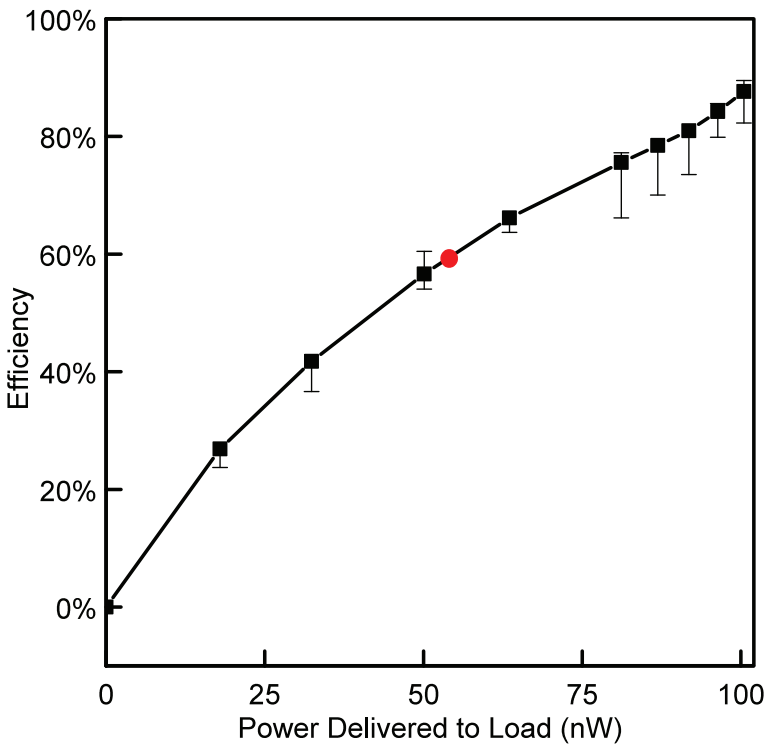


Figure 4.7: Converter efficiency as a function of load power. The red dot marks the operating point of the converter when it is attached to the biocell.

# Chapter 5

# Power Up an Integrated Circuit Using ATP as Fuel Source

## 5.1 Introduction

With the biocell and CMOS IC detailed in the previous chapters, we are now prepared to assemble the hybrid biological solid-state system. The data in this chapter demonstrates that the electrical energy generated by the biocell can be used to power up the CMOS IC. As part of the analysis, this chapter also contains a generalized circuit model for the ATPases that can be used to calculate the conversion efficiency of ATP to electrical power.

## 5.2 Powering a CMOS IC Using the Biocell

### 5.2.1 Mismatched Power Densities

Solid-state systems and biological systems are also mismatched in power density. In general, integrated circuits, even when operated at the point of minimum energy in

subthreshold, consume on the order of $10^{-2}$ W/mm$^2$ (or assuming a typical silicon chip thickness of 250 $\mu$m, $4 \times 10^2$ W/mm$^3$) [61]. Typical cells, in contrast, consume on the order of 4×10 6 W/mm3 [62]. This discrepancy can only be managed through duty cycled operation of the IC in which the circuit is largely disabled for long periods of time. which is then expended in a very brief period of activity.

### 5.2.2 Description of Operation

The discrepancy between available power from the biocell and the minimum requirements of the IC, is managed by harvesting energy from the biocell on a capacitor, $C_{STOR}$ over a period of time, $T_{charge}$, which is then expended subsequently used to power the chip during $T_{run}$. In addition, it was necessary to stack two biocells in series to achieve the minimum voltage for 'self-startup.' The circuit model is shown in figure 5.1 and the data is shown in figure 5.2.

Under duty-cycled operation (after the intial charging cycle), the pump current charges $C_{STOR}$. Figure 5.1(a) shows $V_m$, the biocell voltage, and $V_out$, the voltage at the output of the voltage doubler, as the system is duty cycled. Once $V_m$ reaches $V_{m-high}$ = 145 mV, switch S closes and the voltage doubler starts up, with $V_out$ reaching 279 mV before drooping with $V_m$ as energy is pulled from $C_{STOR}$ (Figure 5.1). Once the voltage on $C_{STOR}$ droops to $V_m = V_{m-low} = 110$ mV, switch S is opened and the biocell begins charging again. The value of $C_{STOR}$, 100 nF in our case, can be determined from $V_{m-high}$, $V_{m-low}$, $R_{IC}$ and $T_{run}$, which yield the allowable droop during the run period, as given by

$$C_{STOR} = \frac{T_{run}}{R_{IC} \ln \left( V_{m-high} / V_{m-low} \right)}. \tag{5.1}$$

The ring-oscillator loads continue to operate for an additional 2.4 ms after S is opened using energy stored on internal-node capacitances. Duty-cycling of the load has the

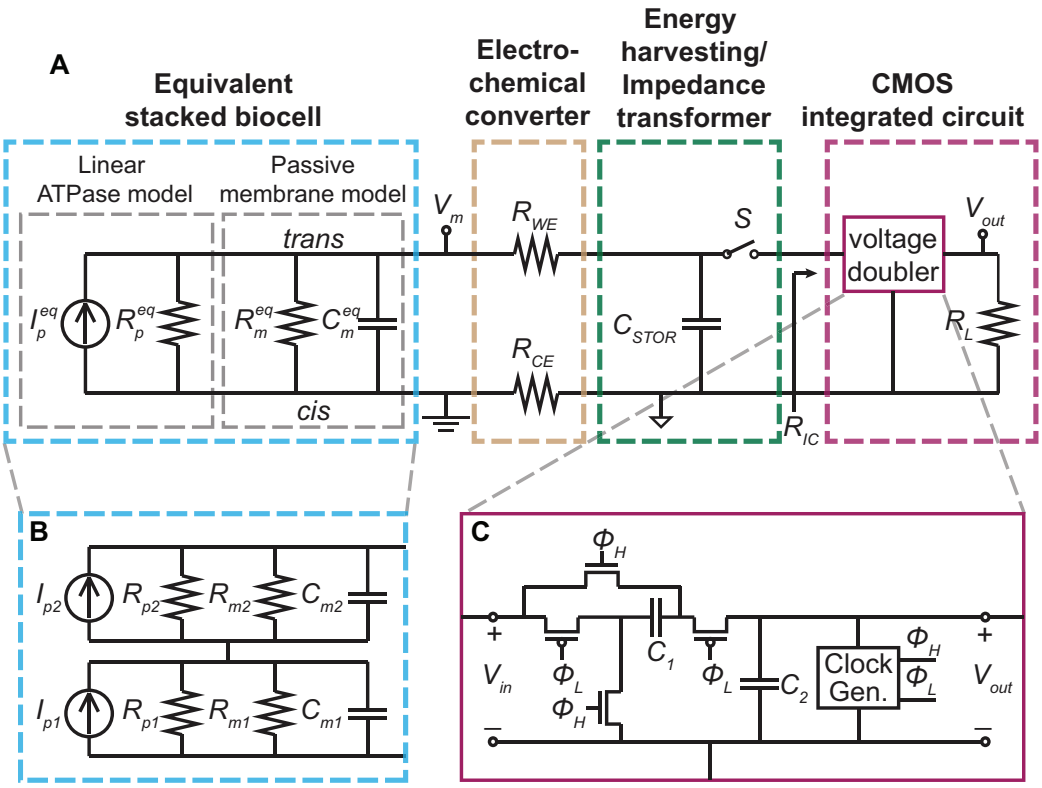


Figure 5.1: Circuit Model of the complete system.

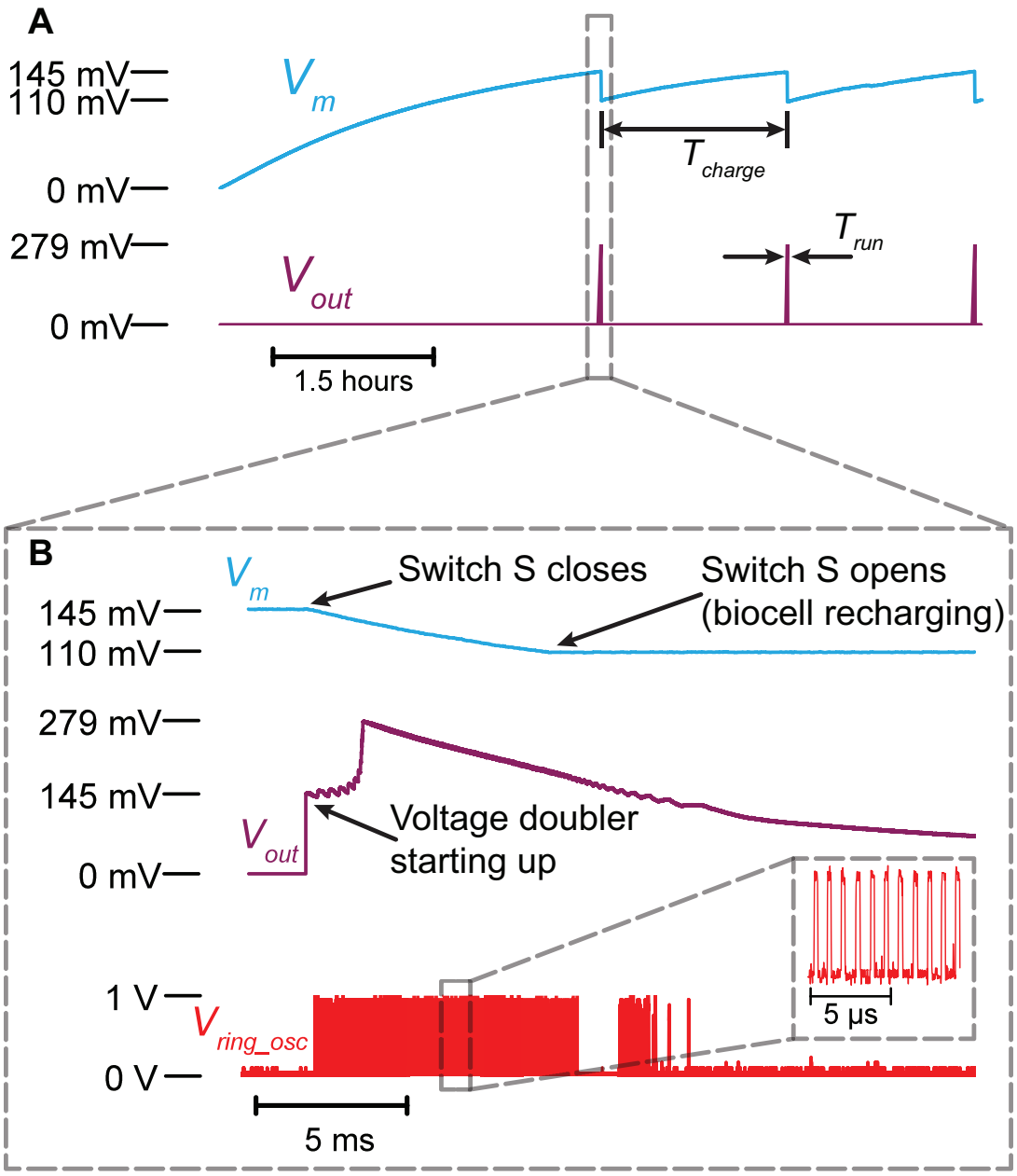


Figure 5.2: Measured data from the chip.

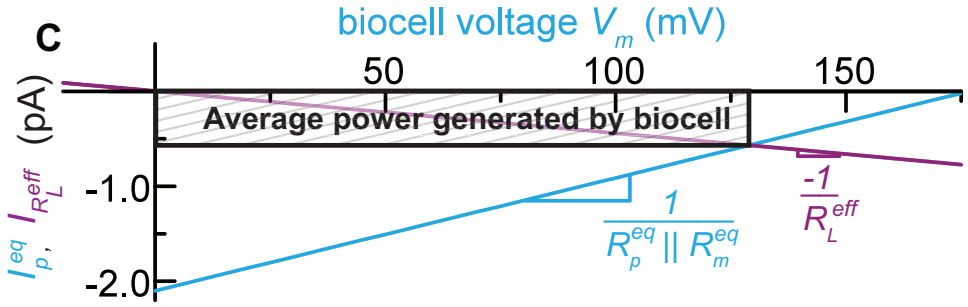


Figure 5.3: Stacked biocell I-V characteristic.

effect of creating a very high effective impedance for loading the biocell, given by

$$R_L^{eff} = R_{IC}\left(\frac{T_{run}}{T_{run} + T_{charge}}\right)^{-1}. \tag{5.2}$$

$R_L^{eff} = 227$ GΩ, which closely matches the optimal impedance for the most efficient energy transfer (derived below). The effective load-line under duty-cycled operation is shown in 5.3 along with the I-V characteristic of the stacked biocell.

## 5.3 Biocell Efficiency Analysis

The overall efficiency of the system in converting chemical energy to the energy consumed in the load ring oscillator ($\eta$) is given by the product of the conversion efficiency of the voltage doubler ($\eta_{converter}$) and the conversion efficiency of chemical energy to electrical energy in the biocell ($\eta_{biocell}$), $\eta_{converter}\eta_{biocell}$. $\eta_{converter}$ was derived in Chapter 4 and is relatively constant over the range of input voltages at 59% +/- 3%, as determined by various loading test circuits. $\eta_{biocell}$, however, varies with transmembrane potential $V_m$.

As reflected in the single membrane circuit model of 5.4 (derived in Chapter 2), $V_m$ in cells is the result of two related potentials, both derived from the action of the ion pumps: the potential which develops as a result of ionic concentration gradients

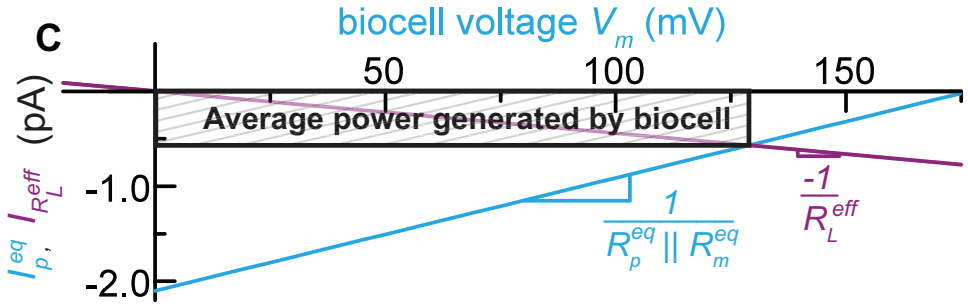


Figure 5.4: Single membrane circuit model.

of membrane permeable ions (the Nernst, or diffusion, potential, $V_{diff}$, maintained by the action of the pumps) and Ohmic potentials ($V_p$) due to the net electrogenic ionic currents of the ion pumps. These combine to determine the membrane potential, $V_m = V_{diff} + V_p$. The diffusion potential, $V_{diff}$, is determined by the superposition of the Thevenin "Nernst" sources for each ionic species, $V_{Na^+}$, $V_{K^+}$, $V_{Mg^{2+}}$, $V_{Cl^-}$, where

$$V_x = \frac{RT}{zF} \ln([X]_{cis}/[X]_{trans}), \tag{5.3}$$

R is the gas constant, T is the absolute temperature, z is the valence of the species, F is Faraday's constant and $[X]_y$ is the concentration of species X in chamber y. A corresponding series resistance $R_X$ models the membrane permeability of those ions present in the system. An equivalent expression for $V_{diff}$ is also given by the Goldman-Hodgkin-Katz (GHK) equation. The total membrane resistance $R_m$ is given by the parallel combination of $R_{Na^+}$, $R_{K^+}$, $R_{Mg^{2+}}$, $R_{Cl^-}$. Using the linear ATPase model, the electrogenic component of the transmembrane potential is given by $V_p = I_p\ (R_p||R_m)$.

To determine $\eta_{biocell}$, we must properly account for the energy harvested from ATP hydrolysis. To accomplish this, we add two voltage sources in series with the non-linear current source $I_{ATPase}$, as shown in 5.5. The additional voltage sources allow us to independently account for the energy expended by the pumps both in

moving charge across the electric potential difference and in moving ions across the chemical potential difference. The dependent voltage source $V_{loss}$ in this branch forces the voltage across the pump dependent current source to be $|\Delta G_{ATP}|/(\mathrm{qN_A})$ where $\Delta G_{ATP}$ is the Gibbs free energy change due to the ATP hydrolysis reaction per mole of ATP at given buffer conditions and $\mathrm{N_A}$ is Avagadro's number). The total power produced by the pump current source $P_{I_{ATPase}}$ is the product of the voltage across the current source and the pump current

$$P_{I_{ATPase}} = \frac{|\Delta G_{ATP}|}{\mathrm{qN_A}} \times \mathrm{q}Nk_{ATP}, \tag{5.4}$$

where $N$ is the total number of functional ATPases in the membrane and $k_{ATP}$ is the rate of ATP hydrolysis per ATPase. The power dissipated in voltage source $V_chem$ models the work performed by the ATPases in transporting ions against a concentration gradient. In the case of the $\mathrm{N^+/K^+}$ ATPase, $V_{chem}$ is given by

$$V_{chem} = 3\frac{\mathrm{R}T}{\mathrm{F}} \ln\left(\frac{[Na^+]_{cis}}{[Na^+]_{trans}}\right) + 2\frac{\mathrm{R}T}{\mathrm{F}} \ln\left(\frac{[K^+]_{trans}}{[K^+]_{cis}}\right). \tag{5.5}$$

The power dissipated in this source is introduced back into the circuit in the power generated by the Nernst independent voltage sources, $V_{Na^+}$ and $V_{K^+}$. The power dissipated in the dependent voltage source $V_{loss}$ models any additional power not used to perform chemical or electrical work.

In our system, no significant ion concentration gradient exists, $V_{chem} = V_{Na^+} = V_{K^+} = V_{Mg^{2+}} = V_{Cl^-} = 0$, and the expanded membrane model of Fig. X becomes the passive membrane model of Fig. X. The stacking of two membranes requires hydrolysis of two molecules of ATP to pump a single charge across the equivalent membrane. Using the linear approximation for $I_{ATPase}$, the efficiency of the biocell is given by

$$\eta_{biocell} = \frac{P_{R_L^{eff}}}{P_{ATP}} = \frac{V_m^2/R_L^{eff}}{\left(2\frac{|\Delta G_{ATP}|}{qN_A}\right)\left(I_p - \frac{V_m}{R_p}\right)} \tag{5.6}$$

and

$$V_{loss} = 2\frac{|\Delta G_{ATP}|}{qN_A} - V_m \tag{5.7}$$

The maximum efficiency occurs at

$$R_L^{eff} = R_m^{eq}\sqrt{\frac{R_p^{eq}}{R_p^{eq} + R_m^{eq}}} \tag{5.8}$$

For the stacked biocell, $R_p^{eq} = 98.6$ GΩ and $R_m^{eq} = 575$ GΩ, $R_L^{eff}$ at maximum efficiency is 220 GΩ with an average $V_m$ of 128 mV. In our system, with $R_L^{eff}$ 227 GΩ, and using a nominal $|\Delta G_{ATP}| = 30$ kJ/mole, $\eta_{biocell} \sim \eta_{biocell}^{max} = 14.9\%$. This yields an overall energy efficiency of the system $\eta = \eta_{converter}\eta_{biocell} = 8.84\%$. In addition, $T_{charge}$ is adjusted dynamically such that the average $V_m \sim V_{m-high}$–$V_{m-low}$ is constant. This has the effect of scaling $R_L^{eff}$ such that $\eta_{biocell}$ is always close to $\eta_{biocell}^{max}$ for any $R_p$ and $R_m$ provided $R_m \gg R_p$ and $R_m \gg R_L^{eff}$.

## 5.4 ATPase Efficiency in Living Systems

Living systems use ATP much more efficiently than in the *in-vitro* system developed here because $V_loss$ is considerably smaller in living systems due to the presence of a non-zero $V_{chem}$. Under typical physiological conditions where the intracellular and extracellular ionic strengths are different, $V_{chem}$ is typically on the order of 336.5 mV at 20 °C [31] with all power lost in $V_{chem}$ converted to electrical power by the voltage sources representing the Nernst potentials of the cell. Higher membrane potentials can be sustained in systems with electrogenic ion pumps engineered with lower $V_{chem}$. For example, proton pumping ATPases, such as those found in the plasma membrane of the yeast S. pombe, transport only a single proton per hydrolyzed molecule of ATP. Less chemical work is performed ($V_{chem} = 14$ mV, for $\Delta$pH = 0.1) compared to the sodium-potassium pumps. As a result, these pumps can sustain a membrane potential of up to 280 mV [63, 64]. In our system, with a similar number of active

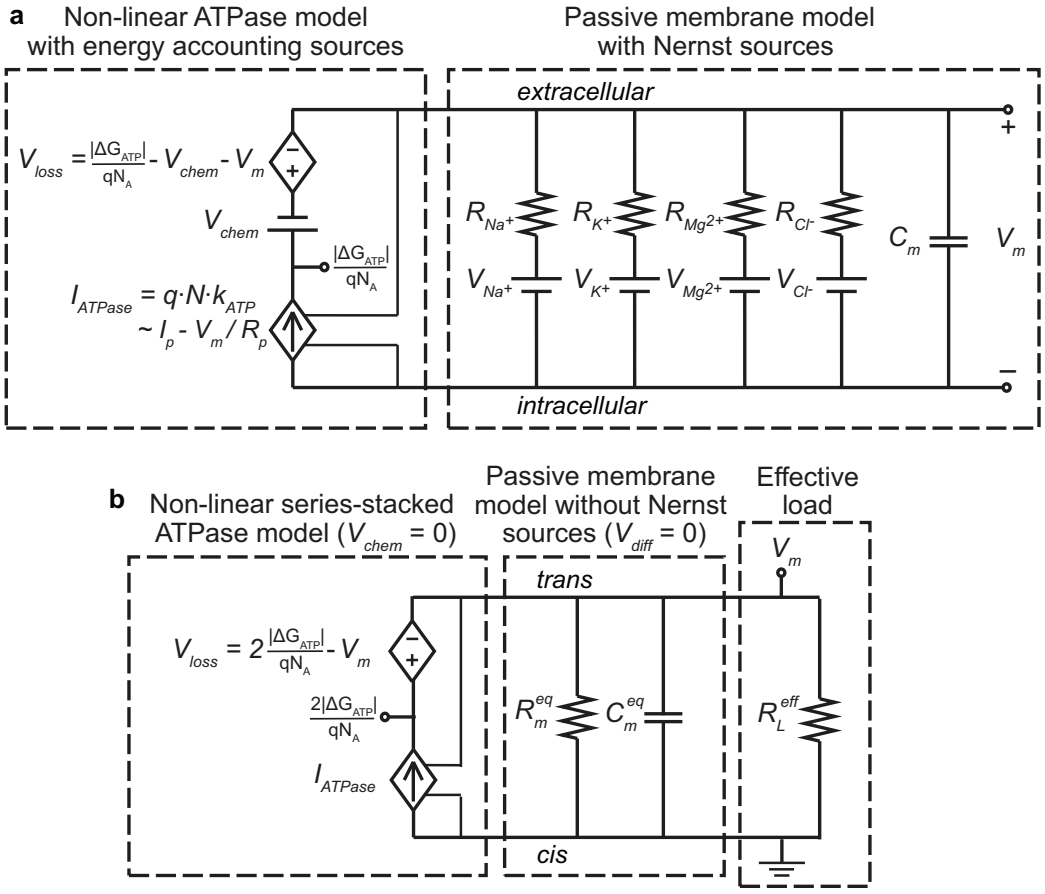


Figure 5.5: ATPase model with energy accounting sources.

incorporated pumps and $R_m$ in excess of 575 G$\Omega$ due to the absence of other channels, voltages of 227 mV could have been achieved with these pumps.

# Chapter 6

# Conclusions

## 6.1 Summary of contributions

This dissertation describes a body of work conducted to integrate an *in-vitro* biological fuel cell which converts ATP into electrical energy to power a CMOS integrated circuit.

This work has made several original contributions to both biology and integrated circuits.

- The first *in-vitro* system containing sodium-potassium pumps in high enough concentration in a membrane of high enough resistance to harvest electrical power.
- A method for photolithographically fabricating hydrophobic wells onto CMOS integrated circuits that can be used as an anchor for artificial membranes.
- An ultra low-power low-voltage integrated circuit with a switched-capacitor voltage doubler for use with biological power sources.
- A novel circuit model that can be used to account for both the chemical and

electrical energy expenditures of ATPases that utilize ATP to pump ions across a membrane.

These contributions have resulted in the following peer-reviewed publications:

- J. M. Roseman, J. Lin, S. Ramakrishnan, J. K. Rosenstein and K. L. Shepard, "Hybrid Biological Solid State Systems: Powering an IC with ATP," Nature Communications, 2015.

- Jaebin Choi, Eyal Aklimi, Jared Roseman, David Tsai, Harish Krishnaswamy, Kenneth L. Shepard, "Matching the power density and potentials of biological systems: a 3.1-nW, 130-mV, 0.023-$mm^3$ pulsed 33-GHz radio transmitter in 32-nm SOI CMOS," Custom Integrated Circuits Conference, 2014.

- J. K. Rosenstein, S. Ramakrishnan, J. Roseman, and K. L. Shepard, "Single ion channel recordings with CMOS-anchored lipid membranes," Nano Letters, 2013.

## 6.2 Future work

This work has laid the foundation for forming hybrid biological-solid-state systems and as a demonstration we have shown that the utilization of a biochemical energy source can be functionally added to a CMOS circuit. There are a few directions in which this work can be taken.

- The large size of the prototype system required that ATP be added manually to the biocell. In order to utilize naturally occurring intracellular ATP, the size of the chip and biocell must be scaled down to fit inside of a cell.

- A second direction, which seeks to add functionality like the senses of taste and smell would require a redesign of the chip which includes an amplifier and the

characterization and integration of ion channels responsible for those senses.

## 6.3 Final thoughts

The hybrid biological-solid-state system presented here has demonstrated that new functionality can be reduced to practice by actively selecting the best components for the task in the biological and solid-state world.

Improvements in this particular system are mentioned above, but ultimately this work could be used as a guide to those wishing to add new functionality to CMOS integrated circuits by integrating subcellular biological components.

# Bibliography

[1] J. P. Changeux, A. Devillers-Thiéry, and P. Chemouilli, "Acetylcholine receptor: an allosteric protein." *Science (New York, N.Y.)*, vol. 225, no. 4668, pp. 1335–1345, 1984.

[2] D. E. Clapham, "TRP channels as cellular sensors." *Nature*, vol. 426, no. 6966, pp. 517–524, 2003.

[3] C. C. Chen, S. England, A. N. Akopian, and J. N. Wood, "A sensory neuron-specific, proton-gated ion channel." *Proceedings of the National Academy of Sciences of the United States of America*, vol. 95, no. 17, pp. 10 240–10 245, 1998.

[4] C. M. Armstrong and B. Hille, "Voltage-gated ion channels and electrical excitability," pp. 371–380, 1998.

[5] D. Branton *et al.*, "The potential and challenges of nanopore sequencing." *Nature biotechnology*, vol. 26, no. 10, pp. 1146–1153, oct 2008.

[6] C. Mead, "Neuromorphic electronic systems," *Proceedings of the IEEE*, vol. 78, no. 10, pp. 1629–1636, 1990.

[7] P. A. Merolla *et al.*, "A million spiking-neuron integrated circuit with a scalable communication network and interface," *Science*, vol. 345, no. 6197, pp. 668–673, 2014. [Online]. Available: http://www.sciencemag.org/cgi/doi/10.1126/science.1254642

[8] A. C. Forster and G. M. Church, "Towards synthesis of a minimal cell." *Molecular systems biology*, vol. 2, p. 45, 2006.

[9] D. G. Gibson *et al.*, "Complete chemical synthesis, assembly, and cloning of a Mycoplasma genitalium genome." *Science (New York, N.Y.)*, vol. 319, no. 5867, pp. 1215–1220, feb 2008.

[10] A. Prindle, P. Samayoa, I. Razinkov, T. Danino, L. S. Tsimring, and J. Hasty, "A sensing array of radically coupled genetic 'biopixels'," *Nature*, vol. 481, no. 7379, pp. 39–44, 2011. [Online]. Available: http://dx.doi.org/10.1038/nature10722

[11] T. Knight, "Idempotent Vector Design for Standard Assembly of Biobricks Idempotent Vector Design for Standard Assembly of Biobricks," *Structure*, pp. 1–11, 2003. [Online]. Available: http://dx.doi.org/http://hdl.handle.net/

1721.1/21168http://dx.doi.org/http://hdl.handle.net/1721.1/21168file:///Y:/MyDocuments/Columbia/papers/biobricks.pdf

[12] F. Bezanilla, "Voltage-Gated Ion Channels," in *Biological Membrane Ion Channels*, S.-H. Chung, O. S. Andersen, and V. Krishnamurthy, Eds. New York, NY: Springer New York, 2007, pp. 81–118. [Online]. Available: http://dx.doi.org/10.1007/0-387-68919-2{_}3http://link.springer.com/10.1007/0-387-68919-2{_}3

[13] L. A. Drachev, A. A. Jasaitis, A. D. Kaulen, A. A. Kondrashin, E. A. Liberman, I. B. Nemecek, S. A. Ostroumov, A. Y. Semenov, and V. P. Skulachev, "Direct measurement of electric current generation by cytochrome oxidase, H+-ATPase and bacteriorhodopsin." *Nature*, vol. 249, no. 5455, pp. 321–324, may 1974. [Online]. Available: http://diyhpl.us/{~}bryan/papers2/bacteriorhodopsin{_}memory/Directmeasurementofelectriccurrentgenerationbycytochromeoxidase,H+-ATPaseandbacteriorhodopsin..pdfhttp://www.nature.com/doifinder/10.1038/249321a0

[14] R. Henderson, "The purple membrane from Halobacterium halobium." *Annual review of biophysics and bioengineering*, vol. 6, no. 4, pp. 87–109, jan 1977. [Online]. Available: http://www.ncbi.nlm.nih.gov/pubmed/326156

[15] J. Berg, J. Tymoczko, and L. Stryer, *Biochemistry*, 5th ed. New York: W. H. Freeman, 2002.

[16] H. Rottenberg, "The measurement of membrane potential and deltapH in cells, organelles, and vesicles." *Methods in enzymology*, vol. LV, no. 1965, 1979. [Online]. Available: http://ukpmc.ac.uk/abstract/MED/37402

[17] C. Wood, C. Williams, and G. J. Waldron, "Patch clamping by numbers," pp. 434–441, 2004.

[18] B. Hille, "Ionic channels in excitable membranes. Current problems and biophysical approaches," *Biophysical Journal*, vol. 22, no. 2, pp. 283–294, 1978. [Online]. Available: http://www.ncbi.nlm.nih.gov/pmc/articles/PMC1473440/

[19] D. B. Caldwell, H. R. Malcolm, D. E. Elmore, and J. a. Maurer, "Identification and experimental verification of a novel family of bacterial cyclic nucleotide-gated (bCNG) ion channels." *Biochimica et biophysica acta*, vol. 1798, no. 9, pp. 1750–6, sep 2010. [Online]. Available: http://www.ncbi.nlm.nih.gov/pubmed/20529663

[20] A. Marty and E. Neher, *Tight Seal Whole-Cell Recording*. Springer Science, 1995. [Online]. Available: http://link.springer.com/10.1007/978-1-4419-1229-9

[21] M. Zagnoni, M. E. Sandison, and H. Morgan, "Microfluidic array platform for simultaneous lipid bilayer membrane formation." *Biosensors & bioelectronics*, vol. 24, no. 5, pp. 1235–40, jan 2009. [Online]. Available: http://www.ncbi.nlm.nih.gov/pubmed/18760585

[22] D. C. Gadsby, "Ion channels versus ion pumps: the principal difference, in principle." *Nature reviews. Molecular cell biology*, vol. 10, no. 5, pp. 344–352, 2009.

[23] A. Bahinski, M. Nakao, and D. C. Gadsby, "Potassium translocation by the Na+/K+ pump is voltage insensitive." *Proceedings of the National Academy of Sciences of the United States of America*, vol. 85, no. 10, pp. 3412–3416, 1988.

[24] P. De Weer, D. C. Gadsby, and R. F. Rakowski, "Voltage dependence of the Na-K pump." *Annual review of physiology*, vol. 50, pp. 225–241, 1988.

[25] P. De Weer and R. F. Rakowski, "Current generated by backward-running electrogenic Na pump in squid giant axons." *Nature*, vol. 309, no. 5967, pp. 450–452, 1984.

[26] J. K. Rosenstein, S. Ramakrishnan, J. Roseman, and K. L. Shepard, "Single ion channel recordings with CMOS-anchored lipid membranes." *Nano letters*, vol. 13, no. 6, pp. 2682–6, jun 2013. [Online]. Available: http://www.ncbi.nlm.nih.gov/pubmed/23634707

[27] C. Himes, E. Carlson, R. J. R. Ricchiuti, B. P. B. Otis, and B. B. A. Parviz, "Ultralow Voltage Nanoelectronics Powered Directly, and Solely, From a Tree," *IEEE Transactions on Nanotechnology*, vol. 9, no. 1, pp. 2–5, jan 2010. [Online]. Available: http://ieeexplore.ieee.org/lpdocs/epic03/wrapper.htm?arnumber=5282623

[28] L. Halámková, J. Halámek, V. Bocharova, A. Szczupak, L. Alfonta, and E. Katz, "Implanted biofuel cell operating in a living snail," *Journal of the American Chemical Society*, vol. 134, no. 11, pp. 5040–5043, 2012. [Online]. Available: http://dx.doi.org/10.1021/ja211714w

[29] P. P. Mercier, A. C. Lysaght, S. Bandyopadhyay, A. P. Chandrakasan, and K. M. Stankovic, "Energy extraction from the biologic battery in the inner ear," *Nature Biotechnology*, vol. 30, no. November, pp. 1240–1243, nov 2012. [Online]. Available: http://www.nature.com/doifinder/10.1038/nbt.2394http://dx.doi.org/10.1038/nbt.2394

[30] Kittel, C. Kittel, and H. Kroemer, *Thermal Physics*. Macmillan, 1980.

[31] S. W. Kuffler, J. G. Nicholls, and A. R. Martin, *From Neuron to Brain: A Cellular Approach to the Function of the Nervous System*. Sinauer, 1984. [Online]. Available: http://books.google.com/books?id=wVxRAAAAMAAJ

[32] A. Y. Kabakov, "Activation of KATP channels by Na/K pump in isolated cardiac myocytes and giant membrane patches." *Biophysical journal*, vol. 75, no. 6, pp. 2858–2867, 1998. [Online]. Available: http://dx.doi.org/10.1016/S0006-3495(98)77728-8

[33] B. Alberts, A. Johnson, J. Lewis, M. Raff, K. Roberts, and P. Walter, *Molecular Biology of the Cell*, 4th ed. New York: Garland Science, 2002.

[34] R. M. Garavito and S. Ferguson-Miller, "Detergents as Tools in Membrane Biochemistry," pp. 32 403–32 406, 2001.

[35] M. R. Villareal, "Cross section of the different structures that phopholipids can take," 2007.

[36] P. Jönsson, M. P. Jonsson, and F. Höök, "Sealing of submicrometer wells by a shear-driven lipid bilayer." *Nano letters*, vol. 10, no. 5, pp. 1900–6, may 2010. [Online]. Available: http://www.ncbi.nlm.nih.gov/pubmed/20405904

[37] A. S. Reddy, D. T. Warshaviak, and M. Chachisvilis, "Effect of membrane tension on the physical properties of DOPC lipid bilayer membrane," *Biochimica et Biophysica Acta (BBA) - Biomembranes*, vol. 1818, no. 9, pp. 2271–2281, sep 2012. [Online]. Available: http://www.sciencedirect.com/science/article/pii/S000527361200154X

[38] P. Mueller, D. O. Rudin, H. T. Tien, and W. C. Wescott, "Reconstitution of cell membrane structure in vitro and its transformation into an excitable system." *Nature*, vol. 194, pp. 979–980, 1962.

[39] B. Martinac, "Mechanosensitive ion channels: molecules of mechanotransduction." *Journal of cell science*, vol. 117, no. Pt 12, pp. 2449–2460, may 2004.

[40] A. Iglic, V. Chandrashekhar, K. Rappolt, and M. Rappolt, *Advances in Planar Lipid Bilayers and Lipsomes*. Elsevier, 2015.

[41] L. K. Tamm and H. M. McConnell, "Supported phospholipid bilayers." *Biophysical journal*, vol. 47, no. 1, pp. 105–13, jan 1985. [Online]. Available: http://www.pubmedcentral.nih.gov/articlerender.fcgi?artid=1435076{\&}tool=pmcentrez{\&}rendertype=abstract

[42] H. Tien and A. Ottova, "Supported planar lipid bilayers (s-BLMs) as electrochemical biosensors," *Electrochimica Acta*, vol. 43, no. 23, pp. 3587–3610, jul 1998. [Online]. Available: http://linkinghub.elsevier.com/retrieve/pii/S0013468698001078

[43] M. Montal and P. Mueller, "Formation of Bimolecular Membranes from Lipid Monolayers and a Study of Their Electrical Properties," *Proceedings of the National Academy of Sciences*, vol. 69, no. 12, pp. 3561–3566, dec 1972. [Online]. Available: http://www.pnas.org/content/69/12/3561.abstract

[44] C. J. Braun, T. Baer, A. Moroni, and G. Thiel, "Pseudo painting/air bubble technique for planar lipid bilayers." *Journal of neuroscience methods*, vol. 233, pp. 13–7, aug 2014. [Online]. Available: http://www.ncbi.nlm.nih.gov/pubmed/24938397

[45] G. Baaken, N. Ankri, A.-K. K. Schuler, J. Rühe, and J. C. Behrends, "Nanopore-based single-molecule mass spectrometry on a lipid membrane

microarray," *ACS Nano*, vol. 5, no. 10, pp. 8080–8088, oct 2011. [Online]. Available: http://www.ncbi.nlm.nih.gov/pubmed/21932787

[46] RCSB, "NKA Rendering." [Online]. Available: http://www.rcsb.org/pdb/explore/explore.do?structureId=3KDP

[47] Hyperphysics, "NKA conformations." [Online]. Available: http://hyperphysics.phy-astr.gsu.edu/hbase/biology/nakpump.html

[48] B. Schuster, D. Pum, O. Braha, H. Bayley, and U. B. Sleytr, "Self-assembled $\alpha$-hemolysin pores in an S-layer-supported lipid bilayer," *Biochimica et Biophysica Acta (BBA) - Biomembranes*, vol. 1370, no. 2, pp. 280–288, mar 1998. [Online]. Available: http://www.sciencedirect.com/science/article/pii/S0005273697002745

[49] H. Alpes, H. J. Apell, G. Knoll, H. Plattner, and R. Riek, "Reconstitution of Na+/K+-ATPase into phosphatidylcholine vesicles by dialysis of nonionic alkyl maltoside detergents," *Biochimica et Biophysica Acta (BBA) - Biomembranes*, vol. 946, no. 2, pp. 379–388, 1988. [Online]. Available: http://www.sciencedirect.com/science/article/pii/0005273688904130

[50] J. K. Rosenstein, M. Wanunu, C. A. Merchant, M. Drndic, and K. L. Shepard, "Integrated nanopore sensing platform with sub-microsecond temporal resolution." *Nature methods*, vol. 9, no. 5, pp. 487–92, may 2012. [Online]. Available: http://www.nature.com/nmeth/journal/v9/n5/abs/nmeth.1932.htmlhttp://www.ncbi.nlm.nih.gov/pubmed/22426489

[51] B. J. Polk, A. Stelzenmuller, G. Mijares, W. MacCrehan, and M. Gaitan, "Ag/AgCl microelectrodes with improved stability for microfluidics," *Sensors and Actuators B: Chemical*, vol. 114, no. 1, pp. 239–247, mar 2006. [Online]. Available: http://linkinghub.elsevier.com/retrieve/pii/S0925400505004612

[52] F. S. Cohen, M. H. Akabas, J. Zimmerberg, and A. Finkelstein, "Parameters affecting the fusion of unilamellar phospholipid vesicles with planar bilayer membranes," *J Cell Biol*, vol. 98, no. 3, pp. 1054–1062, 1984.

[53] S. H. White, "A Study of Lipid Bilayer Membrane Stability Using Precise Measurements of Specific Capacitance," *Biophysical Journal*, vol. 10, no. 12, pp. 1127–1148, 1970. [Online]. Available: http://www.ncbi.nlm.nih.gov/pmc/articles/PMC1367993/

[54] D. C. Gadsby, J. Kimura, and A. Noma, "Voltage dependence of Na/K pump current in isolated heart cells." *Nature*, vol. 315, no. 6014, pp. 63–65, 1985.

[55] G. Wang *et al.*, "A 0.127 um2 High Performance 65nm SOI Based embedded DRAM for on-Processor Applications," in *Electron Devices Meeting, 2006. IEDM '06. International*, 2006, pp. 1–4.

[56] L. Chang, R. K. Montoye, B. L. Ji, A. J. Weger, K. G. Stawiasz, and R. H. Dennard, "A fully-integrated switched-capacitor 2:1 voltage converter with regulation capability and 90% efficiency at 2.3A/mm2," in *VLSI Circuits (VLSIC), 2010 IEEE Symposium on*, 2010, pp. 55–56.

[57] O. Abutbul, A. Gherlitz, Y. Berkovich, and A. Ioinovici, "Step-up switching-mode converter with high voltage gain using a switched-capacitor circuit," *Circuits and Systems I: Fundamental Theory and Applications, IEEE Transactions on*, vol. 50, no. 8, pp. 1098–1102, 2003.

[58] M. Makowski and D. Maksimovic, "Performance limits of switched-capacitor DC-DC converters," in *Proceedings of PESC '95 - Power Electronics Specialist Conference*, vol. 2. IEEE, 1995, pp. 1215–1221. [Online]. Available: http://ieeexplore.ieee.org/lpdocs/epic03/wrapper.htm?arnumber=474969

[59] D. Maksimovic and S. Dhar, "Switched-capacitor DC-DC converters for low-power on-chip applications," in *Power Electronics Specialists Conference, 1999. PESC 99. 30th Annual IEEE*, vol. 1, 1999, pp. 54–59 vol.1.

[60] F. Assaderaghi, D. Sinitsky, S. Parke, J. Bokor, P. K. Ko, and H. Chenming, "A dynamic threshold voltage MOSFET (DTMOS) for ultra-low voltage operation," in *Electron Devices Meeting, 1994. IEDM '94. Technical Digest., International*, 1994, pp. 809–812.

[61] A. A. Demkov and A. Navrotsky, *Materials fundamentals of gate dielectrics*. Springer, 2005, vol. 9.

[62] V. V. Zhirnov and R. K. Cavin III, *Microsystems for bioelectronics: the nanomorphic cell*. William Andrew, 2010.

[63] T. Imai and T. Ohno, "Measurement of yeast intracellular pH by image processing and the change it undergoes during growth phase," *Journal of Biotechnology*, vol. 38, no. 2, pp. 165–172, 1995. [Online]. Available: http://www.sciencedirect.com/science/article/pii/0168165694001305

[64] W. Ziegler, C. L. Slayman, and C. P. Cartwright, "Reconstitution of a plasma-membrane H(+)-ATPase into bilayer lipid membrane." *General physiology and biophysics*, vol. 12, no. 5, pp. 429–43, oct 1993. [Online]. Available: http://www.gpb.sav.sk/1993/1993{_}05{_}429.pdfhttp://www.ncbi.nlm.nih.gov/pubmed/8181690